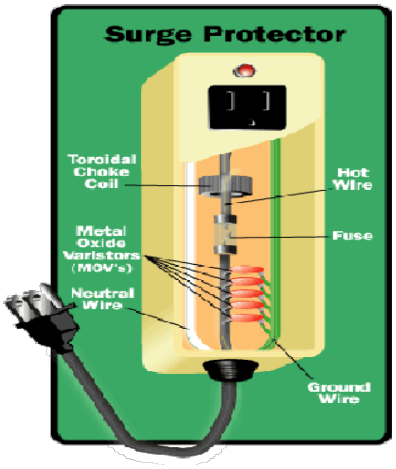

Chapter 5

Electrical and Structural Characterization of Nb_2O_5 Doped ZnO – V_2O_5 Varistor Ceramics Sintered at Different Temperatures.

Chapter 5

Electrical and Structural Characterization of Nb_2O_5 Doped Zno–V_2O_5 Varistor Ceramics Sintered at Different Temperature.

The present chapter addresses the effect of Nb_2O_5 doping on electrical and strutural properties of ZnO-V_2O_5 based varistor ceramics. The current chapter is divided into following two sections: -

Section 1: This section of the chapter describes synthesis of Nb_2O_5 doped ZnO-V_2O_5 based varistor ceramics systems sintered at 850°C, 900°C and 950°C and their structural characterization using XRD, SEM and EDS.

Section 2: Second section discusses the influence of the grain boundaries structure on the electrical properties of ZnO based ceramics in a systematic manner using AC impedance and dieclctric spectroscopy (IS). Various properties investigated include non-linear coefficent, breakdown field, leakage current density, breakdown voltage per grain boundary, ε', tan δ and grain boundary resistance.

Overview: Classical ZnO–Bi_2O_3 and ZnO–Pr_6O_{11} based varistor systems [Levinson et al. (1975)] cannot be co-fired with a pure silver inner-electrode in multilayered chip varistors because of the high sintering temperature (above 1000 °C) in excess of the melting point of silver (Ag mp 961°C). ZnO–V_2O_5 based ceramics can be well sintered at approximately 900 °C. This outstanding feature makes the ZnO–V_2O_5 based varistor a potential candidate for the fabrication of a multi-layered chip varistor using pure silver as inner electrode instead of the expensive palladium or platinum metals.

However, the binary ZnO–V_2O_5 ceramics system exhibit a low nonlinear coefficient (α) [Tsai et al. (1994,1996)]. To improve the nonlinear properties and stability, different metal oxide doped ZnO–V_2O_5 varistor ceramics have been

actively studied until now [Hng et al. (1999, 2000); Nahm et al. (2007, 2009, 2011 & 2015)]. The electrical performances of ZnO varistors critically depend on the microstructure characteristics, where the electrical characteristics can be controlled by modifying the microstructure at the grain boundary. The nonlinear characteristics are attributed to the formation of Double Schottky Barriers (DSB) at the ZnO grain boundaries. Therefore, there are numerous studies addressing the grain boundary phenomena of ZnO-Bi_2O_3 [West et al. (1997); Pandey et al. (2007); Chen et al. (2015)] and ZnO-V_2O_5 based ceramics systems [Wu et al. (2011, 2012)]. It is vital to understand the mechanism controlling the grain boundary processes of ZnO varistor based ceramics. It may also facilitate a researcher or manufacturer to tailor the grain boundary behaviour of ZnO based varistor ceramics in a more efficient manner according to the specific demands of applications. The grain boundary behaviour can be strongly dependent on the dopants. Chen et al. (2015) found that the values of the breakdown field E_{1mA} and nonlinear coefficient are strongly dependent on the resistivity of the grain boundary. Wu et al. (2012) studied the influence of MnO_2, PbO and a mixture of MnO_2, PbO and B_2O_3 on the electrical and dielectric properties of ZnO–V_2O_5 ceramics by impedance and dielectric spectroscopy and found that the schottky barrier present at the grain boundary is significant for varistor performance. Tsai et al. (1994, 1996) found no debye relaxation peak at room temperature for the ZnO–V_2O_5 based ceramics. Therefore, it is necessary that Nb_2O_5 doped ZnO–V_2O_5 ceramics will be studied in term of grain boundary behaviour to tailor multi-layered chip varistors.

5.1. Synthesis and structural behavior of Nb_2O_5-doped ZnO–V_2O_5 varistor.

Reagent grade high purity Sigma Aldrich: ZnO (99.00%), V_2O_5 (99.60%) and Nb_2O_5 (99.99%) were used as raw materials. To investigate the effect of Nb_2O_5 addition, five compositions (99.50 - x) mol% ZnO + 0.5 mol% V_2O_5+ x – mol% Nb_2O_5 (where x = 0.00, 0.05, 0.10, 0.25 and 0.50) were prepared using solid state reaction method. The compositions chosen and the sintering conditions used for each varistor composition are summarized in Tables 5.1, 5.2 and 5.3. All the compositions were mixed homogeneously by conventional ball milling using zirconia balls with acetone in a poly-propylene bottle for 24 h. Thereafter, the mixtures were filtered, dried and calcined at 650 ºC for 3 h. The agglomerates were pulverized using an agate mortar-pestle followed by uniaxially pressed into pellets with of 12.50 mm diameters and 1.25 mm thickness in a hydraulic press at a pressure of 150 MPa using polyvinyl butyral (PVB) as a binder. The pellets were covered with protecting powder and placed inside a closed double alumina crucible at sintering temperature of 850 °C, 900 °C and 950 °C for a soaking period of 3h with both heating and cooling rate of 3°C/min.

Before electrical measurements, the sintered pellets were polished with emery paper on both the sides and then annealed at 700 ºC for 5 h to stabilize the electrical properties. High temperature conductive silver paste was used to coat both faces of the pellets, and the electrodes were formed by curing the paste at 600 °C for 10 min.

A ***nomenclature*** e.g. 850N010 is given to each sample. Here ‘850’ denote the sintering temperature in °C, ‘N’ denotes Nb_2O_5, ‘010’ denotes the mole percent of niobium oxide as 0.10 mol%. Tables 5.1, 5.2 and 5.3 shows the nomenclature of samples.

Table 5.1: Summary of samples composition and their nomenclature, sintered density 'ρ'and average grain size for samples sintered at 850°C for 3h

Sample name	Composition: (Sintered at 850°C for 3hours)			Sintered density (gm/cc)	Average grain size (μm)
	ZnO (mol%)	V_2O_5 (mol%)	Nb_2O_5 (mol%)		
850N000	99.50	0.50	0.00	5.30	5.8
850N005	99.45	0.50	0.05	5.31	5.1
850N010	99.40	0.50	0.10	5.32	5.2
850N025	99.25	0.50	0.25	5.33	5.2
850N050	99.00	0.50	0.50	5.30	5.1

Table 5.2: Summary of samples composition and their nomenclature, sintered density 'ρ' and average grain size for samples sintered at 900°C for 3h

Sample name	Composition: (Sintered at 900°C for 3hours)			Sintered density (gm/cc)	Average grain size (μm)
	ZnO (mol%)	V_2O_5 (mol%)	Nb_2O_5 (mol%)		
900N000	99.50	0.50	0.00	5.49	8.4
900N005	99.45	0.50	0.05	5.43	5.9
900N010	99.40	0.50	0.10	5.43	7.0
900N025	99.25	0.50	0.25	5.41	7.3
900N050	99.00	0.50	0.50	5.37	11.0

Table 5.3: Summary of samples composition and their nomenclature, sintered density 'ρ' and average grain size for samples sintered at 950°C for 3h

Sample name	Composition: (Sintered at 950°C for 3hours)			Sintered density (gm/cc)	Average grain size (μm)
	ZnO (mol%)	V_2O_5 (mol%)	Nb_2O_5 (mol%)		
950N000	99.50	0.50	0.00	5.48	16.6
950N005	99.45	0.50	0.05	5.42	13.5
950N010	99.40	0.50	0.10	5.43	14.9
950N025	99.25	0.50	0.25	5.43	14.7
950N050	99.00	0.50	0.50	5.41	15.5

5.1.1. X-Ray Diffraction (XRD)

The strong and sharp diffraction peaks of the XRD pattern of ZnO varistors sintered at 850 °C, 900 °C and 950 °C are shown in Figs. 5.1, 5.2 and 5.3 respectively and demonstrate that the products are well crystalline. Diffraction peaks present in the XRD patterns of different specimens were matched with the XRD - JCPDS files of constituent phases and other compounds which might have formed during sintering. It has been found that peaks in the XRD patterns matched with JCPDS files of hexagonal ZnO (file no. 361451). Calculation of crystallite size from the measurement of FWHM of XRD peaks of different phases using Scherer formula was calculated for different samples. From the calculated values, it was found that the crystallite size of ZnO (002) plane lies in the range of 51-65 nm. Fig. 5.1 shows XRD patterns of the samples (a) 850N000, (b) 850N005, (c) 850N010, (d) 850N025 and (e) 850N050 sintered at 850°C for 3 hrs. For all of the samples doped with Nb_2O_5, apart from the major ZnO phase, $Zn_3(VO_4)_2$ (JCPDS card no. 191470, 191468 and 340378) was detected as minor secondary phase formed at the grain boundaries and the triple point junction. The secondary phases were produced by the following chemical reaction: $3ZnO + V_2O_5 \rightarrow Zn_3(VO_4)_2$. The major peaks could be indexed as reflections from planes (100), (002), (101), (102) and (110) of hexagonal ZnO. These were identified by comparing with standard JCPDS card no. 361451.The lattice parameters, percentage theoretical density (T.D) and the crystallite D (nm) size for the (002) plane of the Nb_2O_5 doped ZnO varistor samples sintered at 850°C is given in the Table 5.4. The peak positions of (002) plane for pure ZnO (JCPDS Card no. 361451), 0.00, 0.05, 0.10, 0.25 and 0.50 mol% doped ZnO-V_2O_5 samples are 34.42, 34.43, 34.48, 34.46, 34.54, 34.46 degree respectively (Table: 5.4). It can be observed from the data that with Nb co-doping, the peak positions of (002) planes shift slightly toward higher angle compared to un-doped ZnO crystal. The crystallite size of (002) plane for ZnO-V_2O_5, 0.05 mol% Nb-doped ZnO-V_2O_5, 0.10 mol% Nb-doped ZnO-V_2O_5, 0.25 mol% doped ZnO-V_2O_5 and 0.50 mol% doped ZnO-V_2O_5 samples sintered at 850°C is obtained as 59.2, 59.2, 53.9, 56.6 and 51.0 nm respectively are given in Table 5.4.

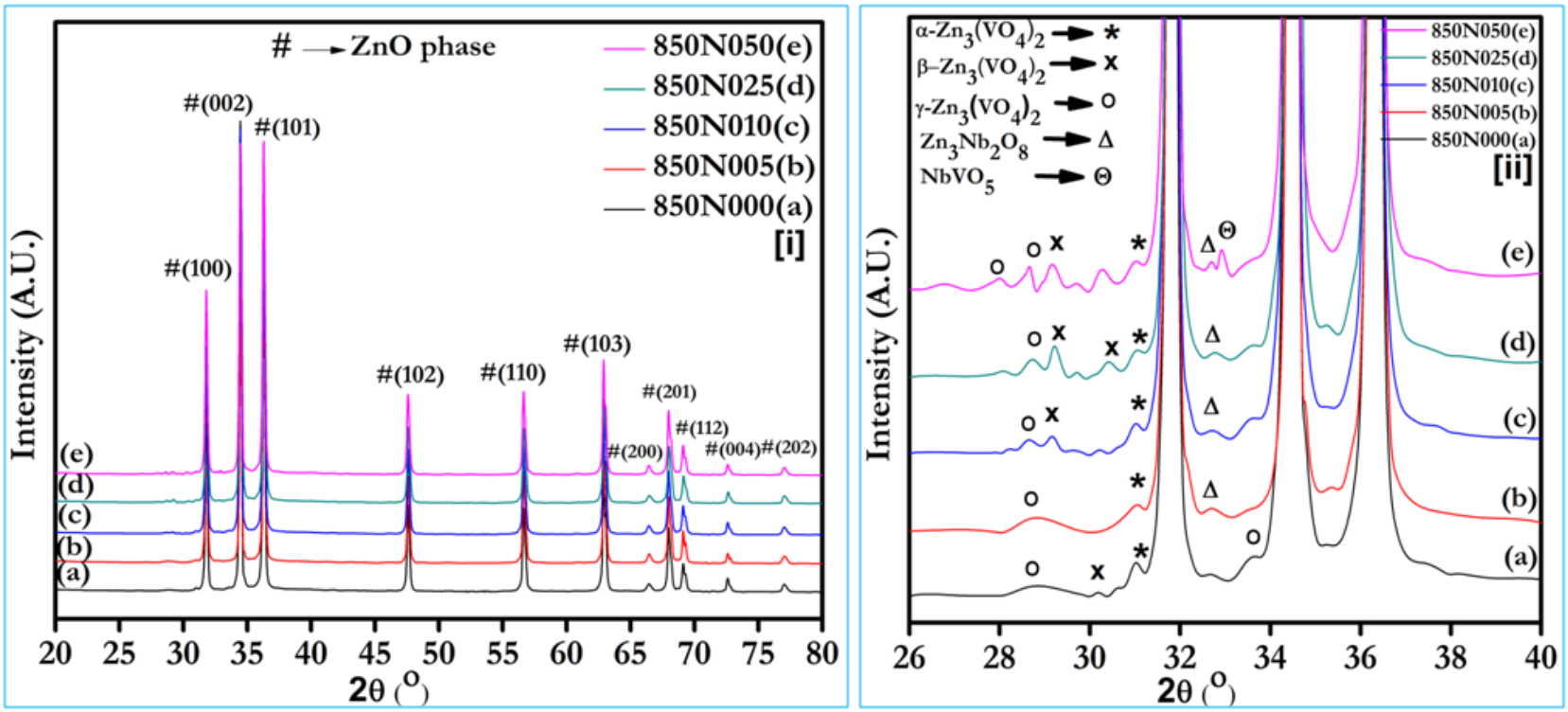

Figure 5.1: X-ray diffraction patterns of samples sintered at 850 °C with following compositions: (a) 850N000 (0.00 mol% Nb); (b) 850N005 (0.05 mol% Nb); (c) 850N010 (0.10 mol% Nb); (d) 850N025 (0.25 mol% Nb) and (e) 850N050 (0.50 mol% Nb).

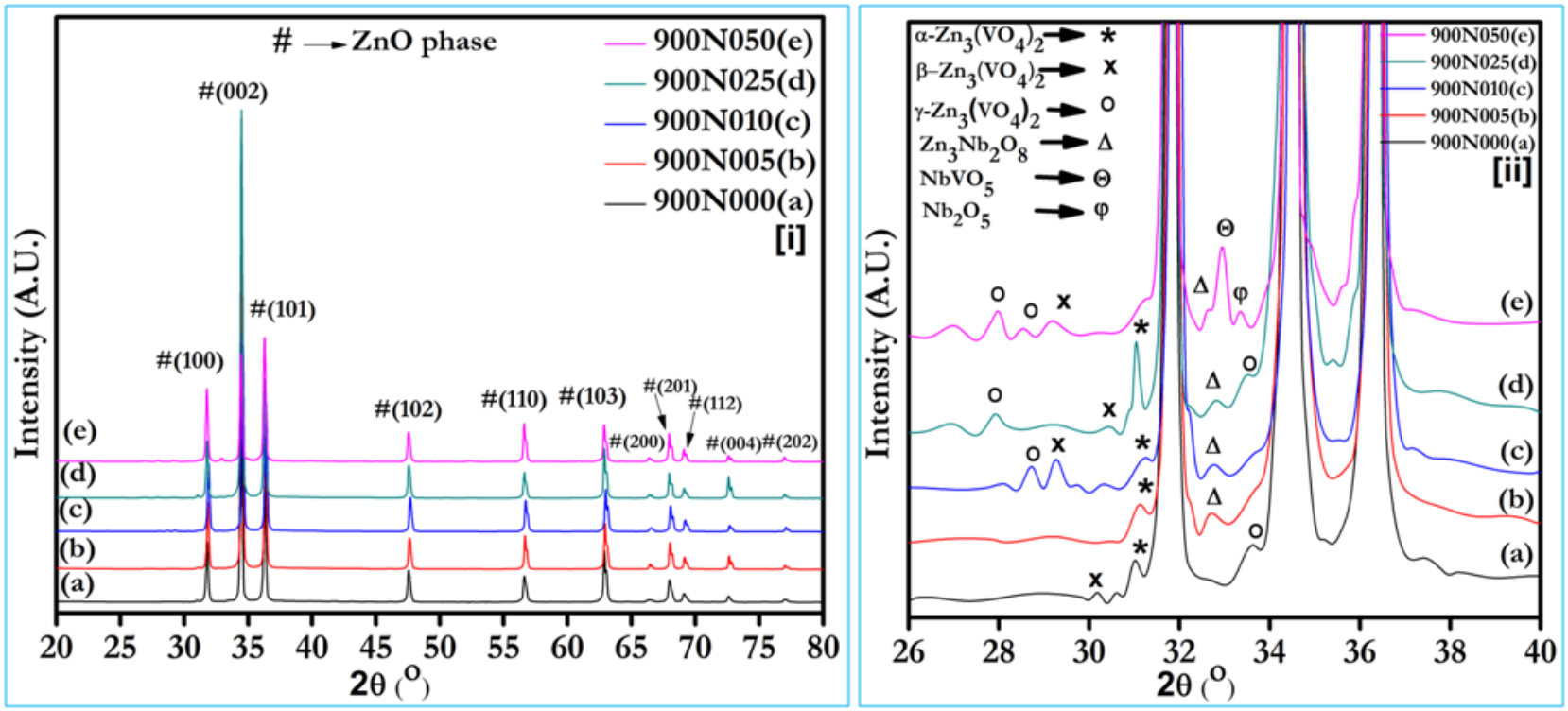

Figure 5.2: X-ray diffraction patterns of samples sintered at 900 °C with following compositions: (a) 900N000 (0.00 mol% Nb); (b) 900N005 (0.05 mol% Nb); (c) 900N010 (0.10 mol% Nb); (d) 900N025 (0.25 mol% Nb) and (e) 900N050 (0.50 mol% Nb).

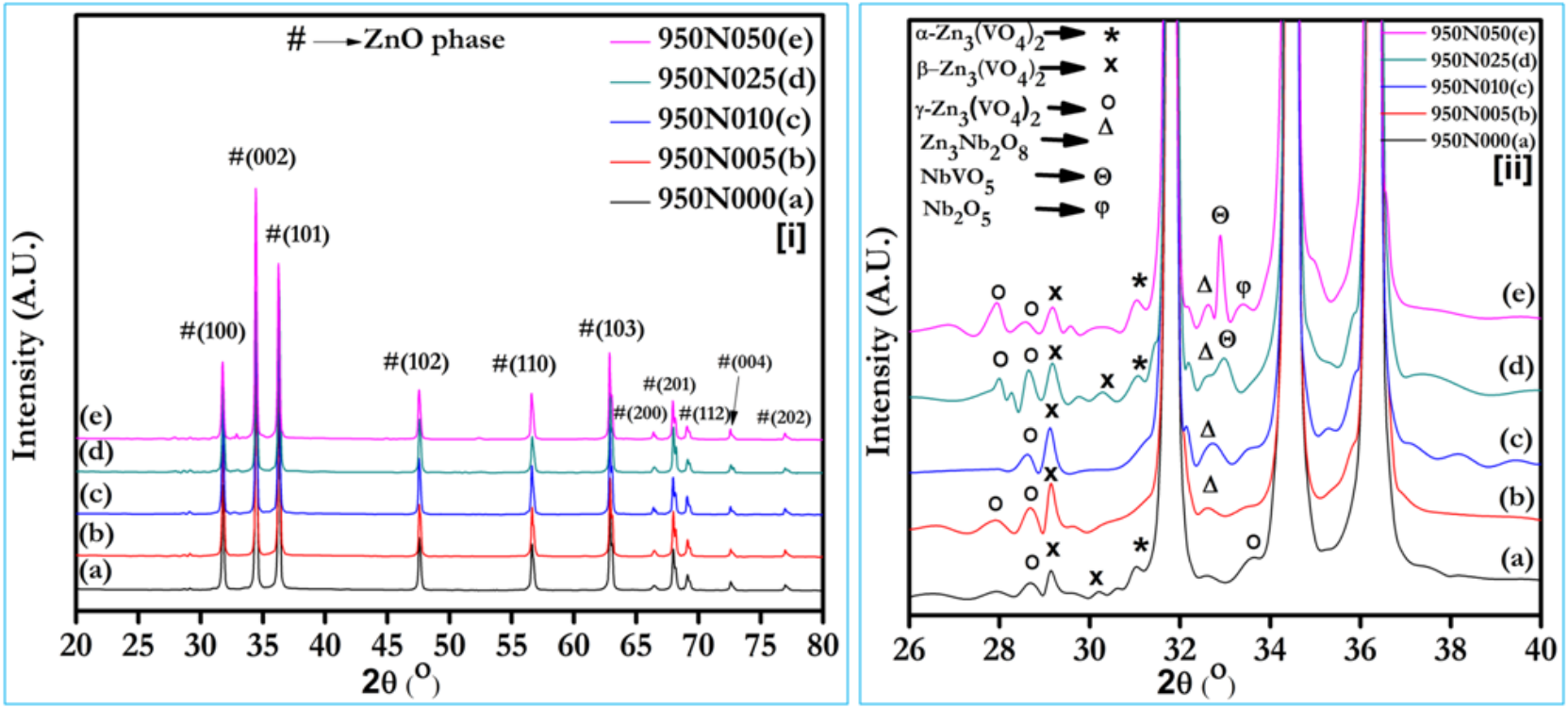

Figure 5.3: X-ray diffraction patterns of samples sintered at 950 °C with following compositions: (a) 950N000 (0.00 mol% Nb); (b) 950N005 (0.05 mol% Nb); (c) 950N010 (0.10 mol% Nb); (d) 950N025 (0.25 mol% Nb) and (e) 950N050 (0.50 mol% Nb).

XRD patterns of the samples (a) 900N000, (b) 900N005, (c) 900N010, (d) 900N025 and (e) 900N050 sintered at 900°C for 3 h are shown in Fig. 5.2. For all of the samples doped with Nb_2O_5, other than the major ZnO phase, $Zn_3(VO_4)_2$ (JCPDS card no. 191470, 191468 and 340378) was detected as minor secondary phases formed at the grain boundaries and the triple point junction. The major peaks could be indexed as reflections from the planes (100), (002), (101), (102) and (110) of hexagonal ZnO. These were identified by comparing with standard JCPDS card no. 361451.The lattice parameters, percentage theoretical density (T.D) and the crystallite size D (nm) for the (002) of the Nb_2O_5 -doped ZnO varistor samples sintered at 900°C is given in Table 5.5.

The peak positions of (002) plane for Pure ZnO (JCPDS Card no. 361451), ZnO-V_2O_5, 0.05 mol% Nb-doped ZnO-V_2O_5, 0.10 mol% Nb-doped ZnO-V_2O_5, 0.25 mol% doped ZnO-V_2O_5 and 0.50 mol% doped ZnO-V_2O_5 samples are 34.42, 34.44, 34.52, 34.56, 34.47, 34.45 (Table: 5.5). It can be observed from the data that with V, Nb co-doping the peak positions of (002) planes shift slightly toward higher angle as compared to pure ZnO crystal. The crystallite size of (002) plane for 0.00, 0.05, 0.10, 0.25 and 0.50 mol% doped ZnO-V_2O_5 samples sintered at 900°C is obtained as 57.2, 63.8, 59.5, 58.7 and 65.8 nm respectively are given in Table 5.5.

Fig. 5.3 shows XRD patterns of the specimens (a) 950N000, (b) 950N005, (c) 950N010, (d) 950N025 and (e) 950N050 sintered at 950 °C for 3 h. For all of the samples doped with Nb_2O_5, apert from the major ZnO phase, $Zn_3(VO_4)_2$ (JCPDS card no. 191470, 191468 and 340378) was detected as minor secondary phase. The major peaks could be indexed as reflections from planes (100), (002), (101), (102) and (110) of hexagonal ZnO. These were identified by comparing with standard JCPDS card no. 361451.The lattice parameters, percentage theoretical density (T.D) and the crystallite size D (nm) for the (002) plane of the Nb_2O_5 -doped ZnO varistor samples sintered at 900°C is given in Table 5.6. The peak positions of (002) plane for Pure ZnO (JCPDS Card no. 361451), ZnO-V_2O_5, 0.05 mol% Nb-doped ZnO-V_2O_5, 0.10 mol% Nb-doped ZnO-V_2O_5, 0.25 mol% doped ZnO-V_2O_5 and 0.50 mol% doped ZnO-V_2O_5 samples are 34.42, 34.45, 34.46,

34.45, 34.46, 34.47 degree respectively (Table: 5.6). It can be observed from the data that with V, Nb co-doping the peak positions of (002) planes shift slightly toward higher angle as compared to un-doped pure ZnO crystal. The crystallite size of (002) plane for ZnO-V_2O_5, 0.05 mol% Nb-doped ZnO-V_2O_5, 0.10 mol% Nb-doped ZnO-V_2O_5, 0.25 mol% doped ZnO-V_2O_5 and 0.50 mol% doped ZnO-V_2O_5 samples sintered at 950 °C are 56.6, 58.1, 60.1, 57.4 and 61.1 degree respectively are given in Table 5.6.

Table 5.4: Lattice parameters, percentage theoretical density (T.D) and crystallite size D (nm) for (002) of Nb_2O_5 doped samples sintered at 850 °C.

Sample name	a = b (A°)	c (A°)	Unit cell volume ($A°^3$)	Percentage theroretical density (T.D)	Crystallite size D (nm) for (002)	2θ° for (002)
ZnO Pure	3.249	5.206	47.591	--	--	34.42
850N000	3.163	5.318	46.075	90.36	59.3	34.43
850N005	3.248	5.202	47.529	92.42	59.2	34.48
850N010	3.249	5.203	47.556	93.54	53.9	34.46
850N025	3.248	5.195	47.422	93.44	56.6	34.54
850N050	3.249	5.202	47.553	93.26	51.0	34.46

Table 5.5: Lattice parameters, percentage theoretical density (T.D) and crystallite size D (nm) of Nb_2O_5 doped samples sintered at 900 °C.

Sample name	a = b (A°)	c (A°)	Unit cell volume ($A°^3$)	Percentage theroretical density (T.D)	Crystallite size D (nm) for (002)	2θ° for (002)
ZnO Pure	3.249	5.206	47.591	--	--	34.42
900N000	3.128	5.307	44.968	91.35	57.2	34.44
900N005	3.247	5.197	47.450	95.32	63.8	34.52
900N010	3.245	5.193	47.355	95.25	59.5	34.56
900N025	3.25	5.204	47.602	95.34	58.7	34.47
900N050	3.248	5.203	47.534	94.42	65.8	34.45

Table 5.6: Lattice parameters, percentage theoretical density (T.D) and crystallite size D (nm) of Nb_2O_5 doped samples sintered at 950 °C.

Sample name	a = b (A°)	c (A°)	Unit cell volume ($A°^3$)	Percentage theroretical density (T.D)	Crystallite size D (nm) for (002)	2θ° for (002)
ZnO Pure	3.249	5.206	47.591	--	--	34.42
950N000	3.118	5.297	46.178	93.67	56.6	34.45
950N005	3.248	5.203	47.535	95.33	58.1	34.46
950N010	3.249	5.206	47.589	95.58	60.1	34.45
950N025	3.249	5.202	47.550	95.64	57.4	34.46
950N050	3.250	5.207	47.625	95.34	61.1	34.47

5.1.2. Scanning Electron Microscopy (SEM)

Fig. 5.4 shows the SEM micrographs of the thermally etched sintered specimens (a) 850N000, (b) 850N005, (c) 850N010, (d) 850N025 and (e) 850N050 sintered at 850 °C for different doping contents of Nb_2O_5 at 10000X magnification (or 10μm scale). Grain size are calculated as 5.88, 5.13, 5.23, 5.16 and 5.08 μm respectively from SEM image. Small, closely spaced anhedral grains were nonuniformly distributed across the sample. Since because of the eutectic temperature for V_2O_5-ZnO is approximately 600 °C, a liquid phase sintering process occurs when the sintering temperature is higher than the eutectic temperature that's lead to grain growth of ZnO and densification of samples. For the samples sintered at 850 °C, the overall trend in the grain growth decreases with the increase of Nb_2O_5 doping concentration. This indicates that Nb_2O_5 act as a grain growth inhibitor. The sample microstructure shown in Fig. 5.4 (a–e) was quite dense, with areas of closed spherical porosity, indicating the sintering process had reached to the final stage. Anisotropic grain growth observed resulting from sintering in the presence of a liquid phase. Overall, it can be seen that the grain size was inhomogeneous, despite clear grain boundaries. The average grain size of the ZnO-V_2O_5 system was found to be 5.88 μm, which decreased to 5.13 μm by addition of 0.05 mol% Nb_2O_5. The ZnO-V_2O_5 doped with 0.10 mol% Nb_2O_5 exhibited the most uniform grain size of 5.23 μm. Further addition of Nb_2O_5 (0.50 mol %) decreased the average grain size to 5.08 μm.

Fig. 5.5 shows the SEM micrographs of the thermally etched sintered specimens (a) 900N000, (b) 900N005, (c) 900N010, (d) 900N025 and (e) 900N050 for different doping contents of Nb_2O_5 at 10000X magnification (or 10μm scale) grain size of 8.41, 5.85, 7.01, 7.31 and 11.01 μm respectively are calculated from SEM image. Microstructures at low magnification shows a dense phase micrograph with small amount of porosity indicating that the sintering process had reached the final stage. Anisotropic grain growth observed resulting from sintering in the presence of a liquid phase.

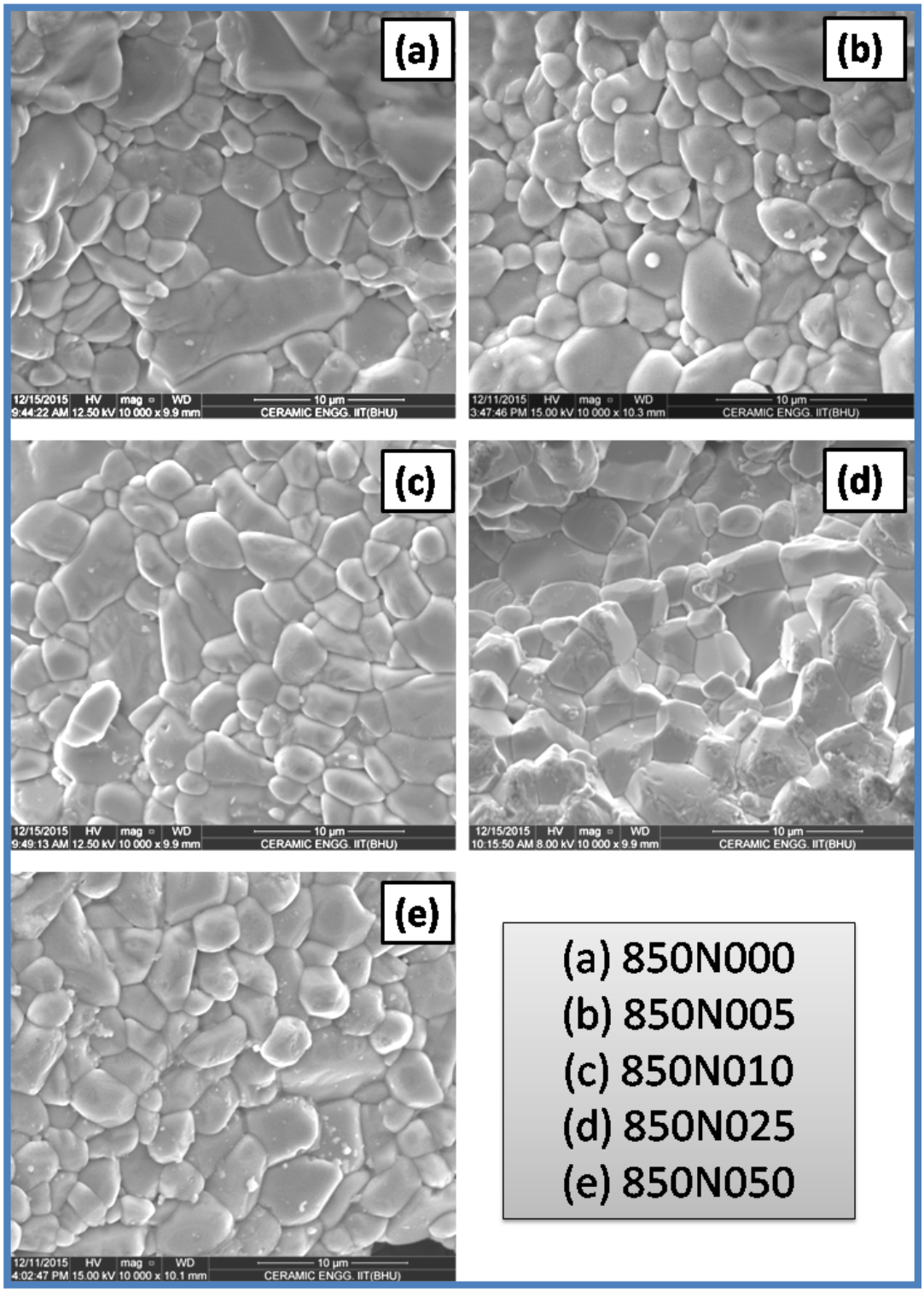

Figure 5.4: SEM micrographs of the sample sintered at 850 °C with following compositions: (a) 850N000 (0.00 mol% Nb); (b) 850N005 (0.05 mol% Nb); (c) 850N010 (0.10 mol% Nb); (d) 850N025 (0.25 mol% Nb); and (e) 850N050 (0.50 mol% Nb).

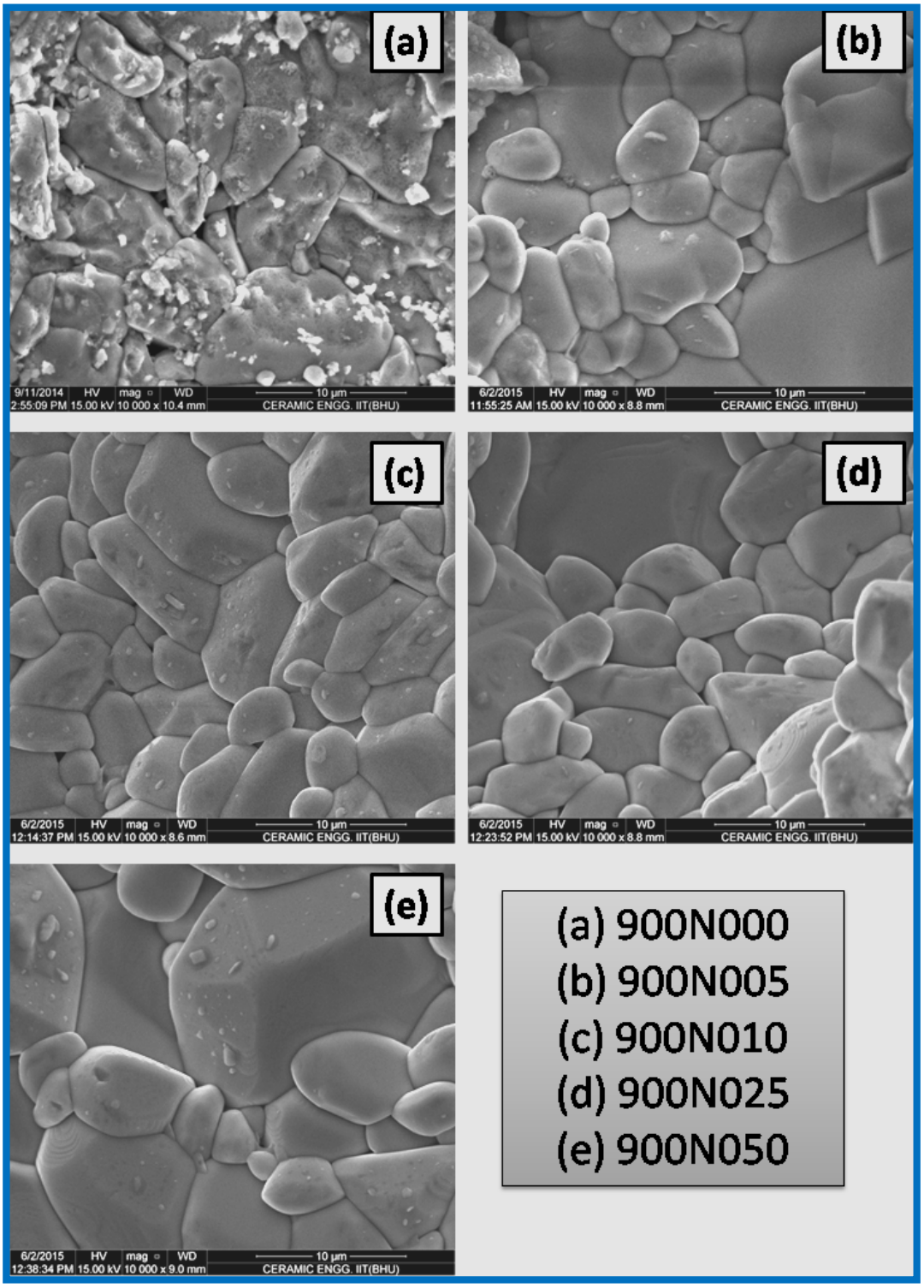

Figure 5.5: SEM micrographs of the samples sintered at 900 °C with following compositions: (a) 900N000 (0.00 mol% Nb); (b) 900N005 (0.05 mol% Nb); (c) 900N010 (0.10 mol% Nb); (d) 900N025 (0.25 mol% Nb); and (e) 900N050 (0.50 mol% Nb).

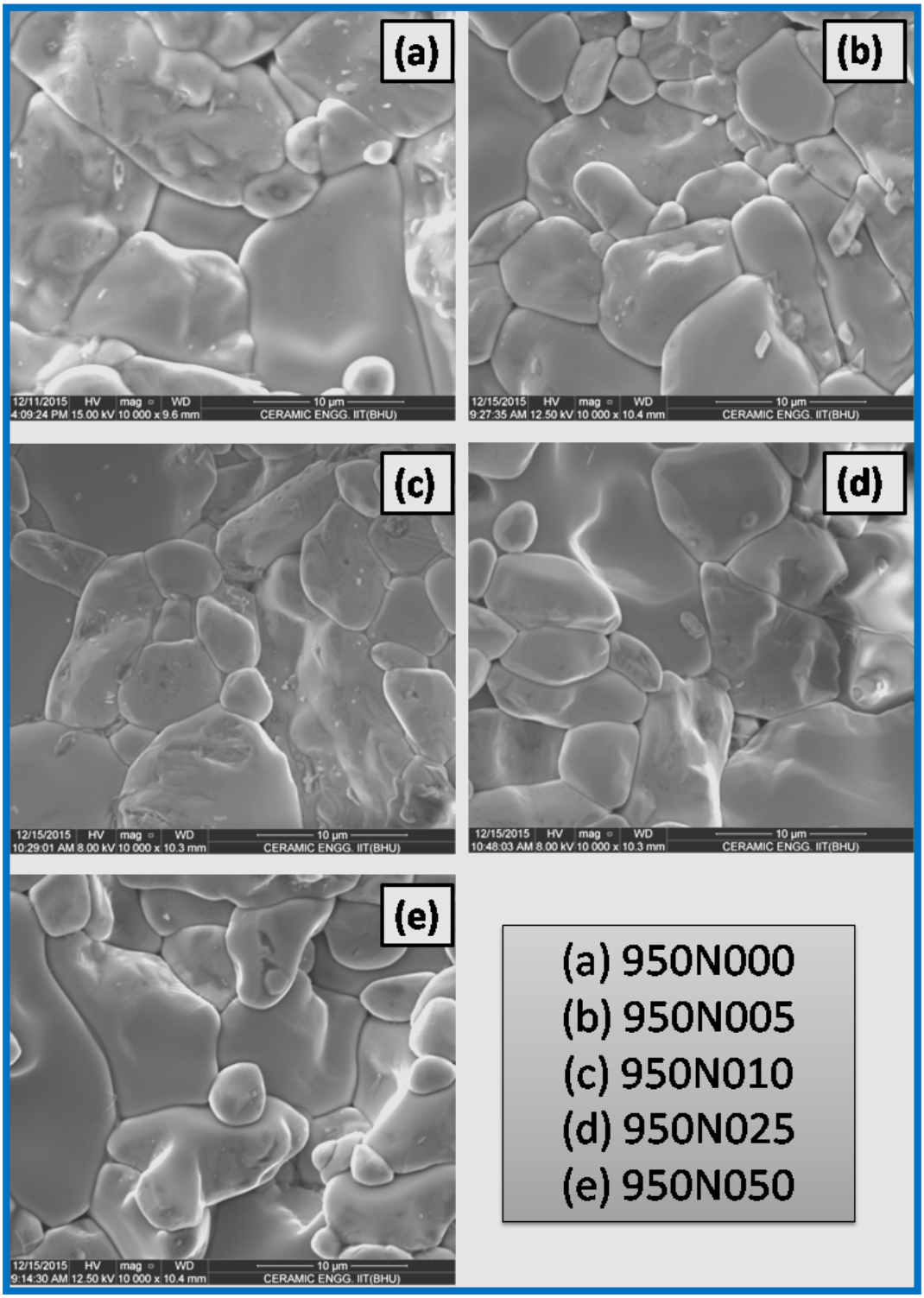

Figure 5.6: SEM micrographs of the samples sintered at 950 °C with following compositions: (a) 950N000 (0.00 mol% Nb); (b) 950N005 (0.05 mol% Nb); (c) 950N010 (0.10 mol% Nb); (d) 950N025 (0.25 mol% Nb); and (e) 950N050 (0.50 mol% Nb)

For the samples sintered at 900 °C, the average grain size of the ZnO-V_2O_5 system was found to be 8.41 μm, which first decresed to 5.85 μm by addition of 0.05 mol% Nb_2O_5 . Further addition of Nb_2O_5 (0.50 mol %) increased the average grain size abnormally to 11.01 μm. The ZnO -V_2O_5 doped with 0.10 mol% Nb_2O_5 exhibited the most uniform grain size of 7.01 μm.

SEM micrographs of the thermally etched sintered specimens (a) 950N000, (b) 950N005, (c) 950N010, (d) 950N025 and (e) 950N050 for different content of Nb_2O_5 at 10000X magnification (or 10μm scale) are shown in Fig. 5.6. Grain size are calculated as 16.64, 13.58, 14.91, 14.72 and 15.54 μm respectively from SEM image. Microstructures at low magnification show a dense phase micrograph with areas of the closed spherical porosity indicating that the sintering process had reached to the final stage. Anisotropic grain growth observed resulting from sintering in the presence of a liquid phase. For the samples sintered at 950 °C. The average grain size of ZnO-V_2O_5 system was found to be 16.64 μm, which first decresed to 13.58 μm by addition of 0.05 mol% Nb_2O_5 . Further addition of Nb_2O_5 (0.50 mol %) increased the average grain size to 15.54 μm. The ZnO-V_2O_5 doped with 0.10 mol% Nb_2O_5 exhibited the most uniform grain size to 14.91 μm. The microstructure observation revealed that the Nb_2O_5 addition retarded the grain growth. At lower concentration, Nb_2O_5 could precipitate together with ZnO along the grain boundaries and participates in lowering the grain size of the doped samples

SEM micrographs of the samples at different Nb_2O_5 content show the following features: (i) the average grain size depends on the niobium content, (ii) there were large grains dispersed in a matrix composed of small grains, (iii) the large grains grew faster than the small grains and (iv) the large grains always had an oblong shape. With respect to the oblong shape of exaggerated grains, it observed that the grain growth in these samples was quite anisotropic.

5.1.3. Energy-dispersive X-ray spectroscopy (EDS)

EDS spectra for sample 900N000 at different regions, especially grain interiors and grain boundaries, are shown in Fig. 5.7. EDS spectra of the ZnO grain boundary reveal V segregation in ZnO-V_2O_5 sample (900N000). Fig. 5.8 shows EDS elemental maps for Zn, O and V of samples with addition of 0.50 mol% V_2O_5 and 99.50 mol% ZnO.

EDS spectra for 0.05 mol% Nb_2O_5 doped ZnO-V_2O_5 (900N005) sample at different regions, especially the grain interior and the grain boundary, are shown in Fig. 5.9 EDS spectra of the ZnO grain boundary shows V and Nb segregation in the sample (900N005). At lower concentration, Nb_2O_5 could precipitate together with ZnO along the grain boundaries and participate in lowering the grain size of the doped samples.

Fig. 5.10 shows EDS elemental maps for Zn, O, V and Nb of the samples with addition of 0.05 mol% Nb_2O_5, 0.50 mol%V_2O_5 and 99.45 mol% ZnO.

EDS spectra for 0.10 mol% Nb_2O_5 doped ZnO-V_2O_5 (900N010) at different regions, especially grain interiors and grain boundaries, are shown in Fig. 5.11. EDS spectra of the ZnO grain boundary reveal V and Nb segregation in the sample 900N010. At lower concentration, Nb_2O_5 could precipitate together with ZnO along the grain boundaries and participates in lowering the grain size of the doped samples.

Fig. 5.12 shows EDS elemental maps for Zn, O, V and Nb of samples with addition of 0.10 mol% Nb_2O_5, 0.50 mol% V_2O_5 and 99.40 mol% ZnO.

EDS spectra for 0.50 mol% Nb_2O_5 doped ZnO-V_2O_5 (900N050) at different regions, especially grain interiors and grain boundaries, are shown in Fig. 5.13. EDS spectra of the ZnO grain boundary reveal V and Nb segregation in the sample 900N050.

Fig. 5.14 shows EDS elemental maps for Zn, O, V and Nb of samples with addition of, 0.50 mol% Nb_2O_5, 0.50 mol% V_2O_5 and 99.00 mol% ZnO.

The grey-scale density in the EDS elemental maps images increases with increasing amount of an element present. V and Nb are present at the grain boundaries and coexist with segregated particles and compound at the triple points in the samples. The XRD and EDS analysis results reveal that V is incorporated in a grain boundary. As indicated in EDS spectra, the components in minor phases are confirmed by using EDS analysis. The minor phases was $Zn_3(VO_4)_2$ containing Nb in the light of the detection of V species. EDS confirms that only Zn, O and Nb are present in the samples. The mass % of Zn and O in each sample was not as per stoichiometric proportion. The entire samples were observed to be oxygen deficient. The sample doped with 0.10 mol% Nb_2O_5 was observed to be oxygen deficient. The deficiency or excess of the constituent material results in distorted band structure with corresponding decrease in resistivity. Zinc oxide loses oxygen on heating so that the zinc is in excess. The oxygen of course evolves as electrically neutral substance so that it is associated with each excess zinc ion in the crystal; there will be two electrons that remain trapped in the solid material, thus leading to non-stoichiometricity in the solid. This leads to the formation of the semiconducting nature of the material.

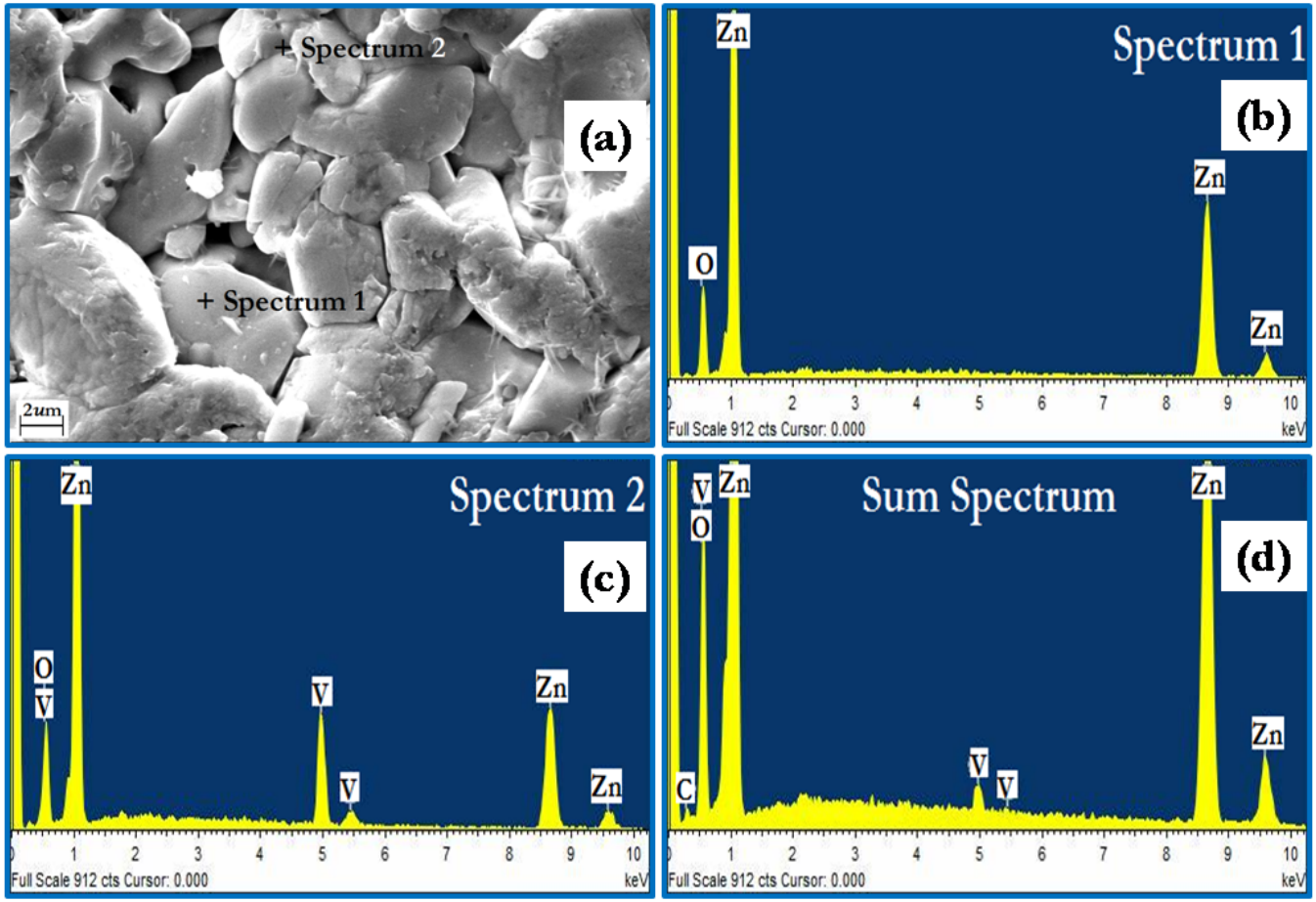

Figure 5.7: EDS spectra of binary ZnO-V_2O_5 (900N000) (a) SEM micrograph (b) at the ZnO grain (c) at the ZnO grain boundary showing V segregation in it and (d) sum spectrum or full frame

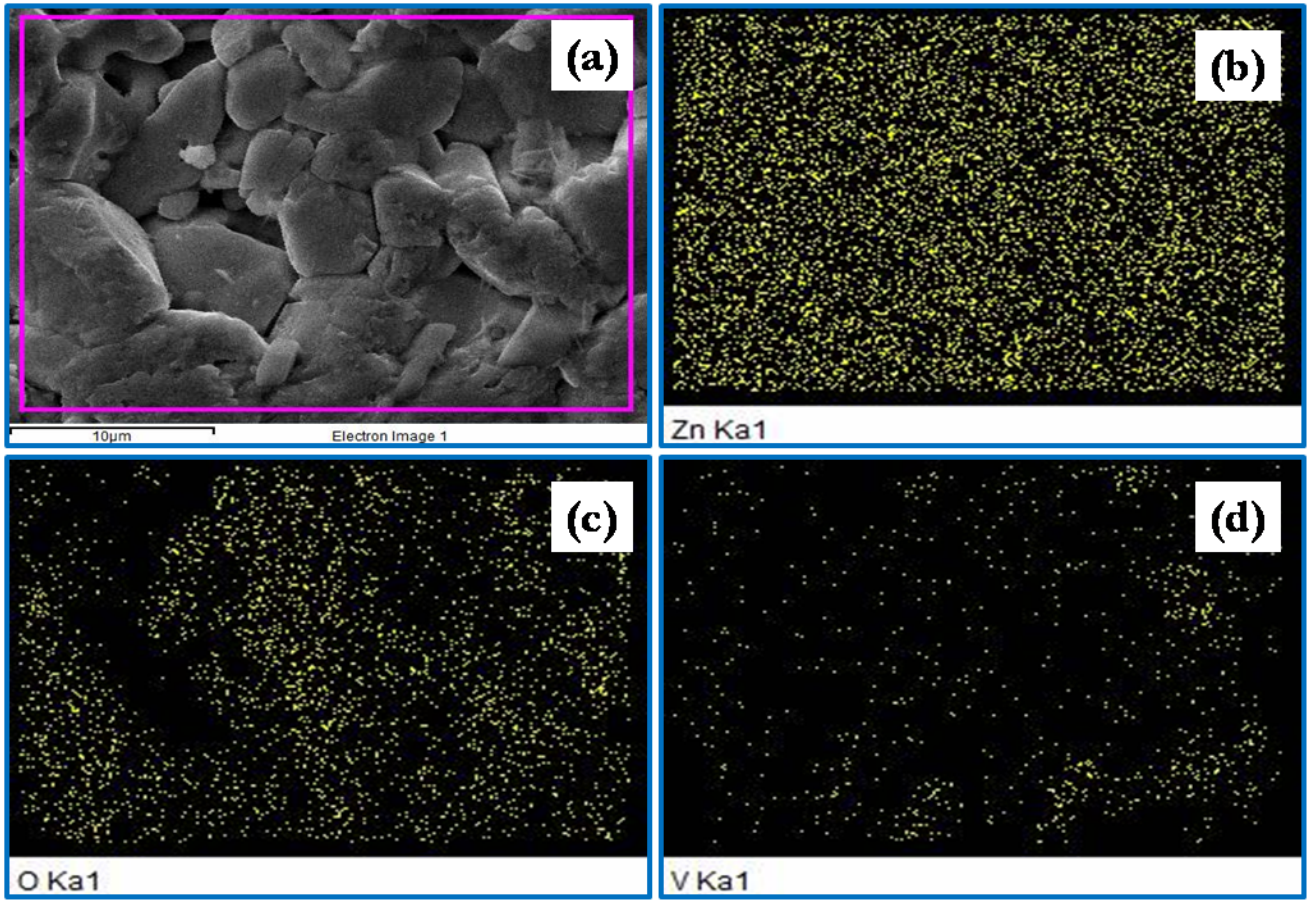

Figure 5.8: EDS elemental maps for binary ZnO-V_2O_5 System (900N000) (a) SEM micrograph (b) Zn map (c) O map and (d) V map.

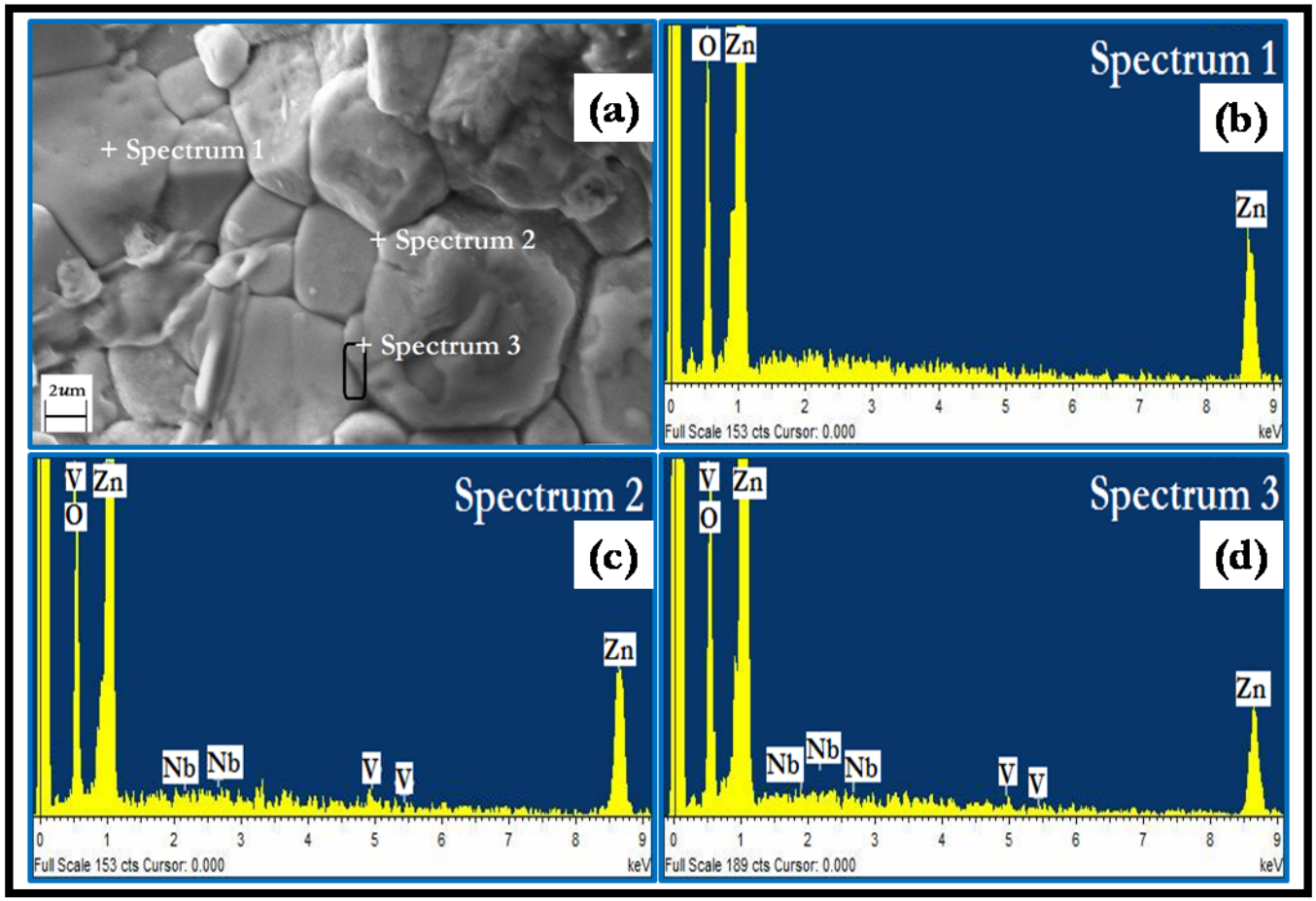

Figure 5.9: EDS spectra of 0.05 mol% Nb doped ZnO-V_2O_5 sample (900N005) (a) SEM micrograph (b) at the ZnO grain (c) at the ZnO grain boundary showing V segregation in it and (d) at the selected region.

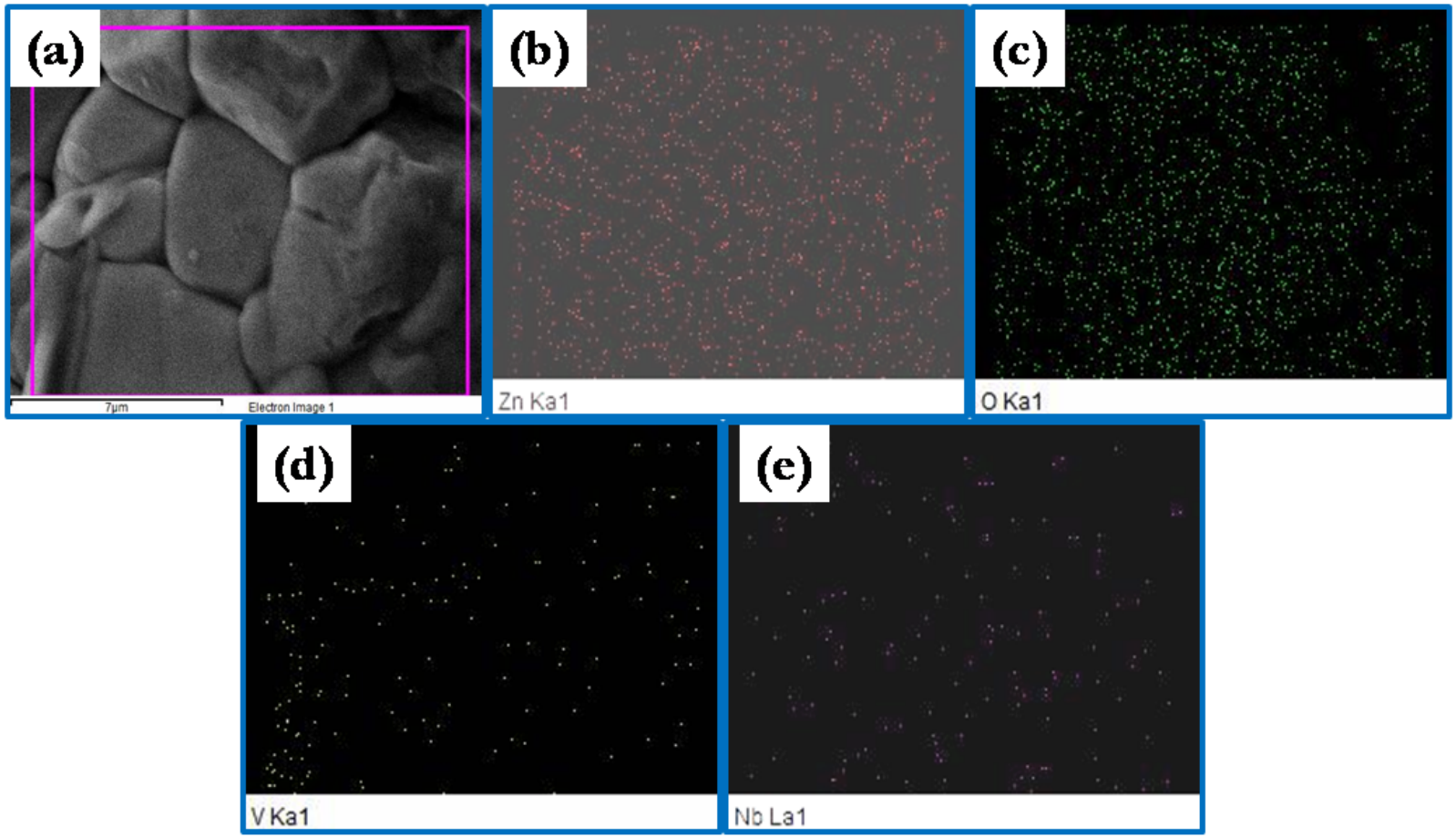

Figure 5.10: EDS elemental maps for 0.05 mol% Nb doped ZnO-V_2O_5 System (900N005): (a) SEM micrograph (b) Zn map (c) O map and (d) V map and (e) Nb map.

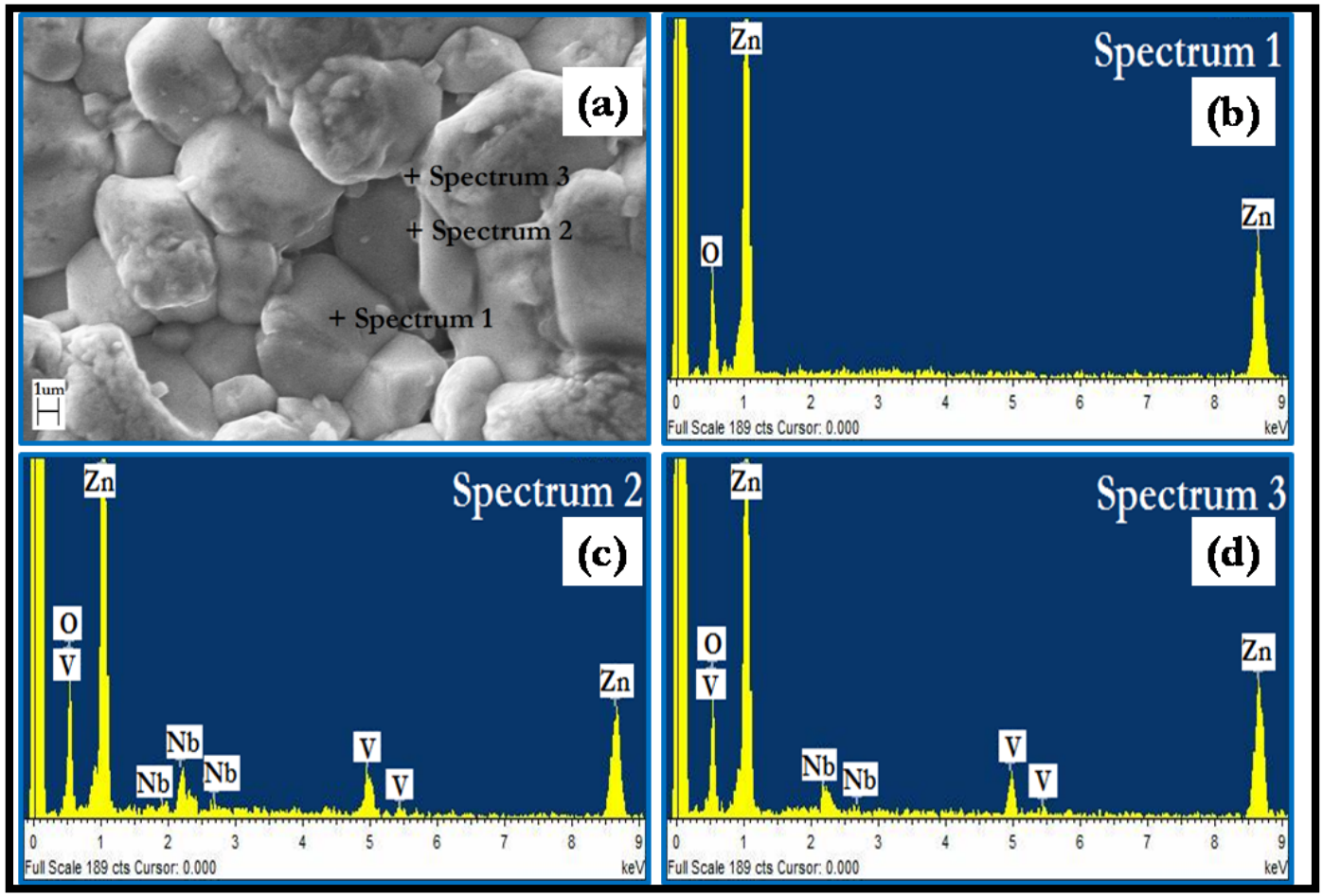

Figure 5.11: EDS spectra of 0.10 mol% Nb doped ZnO-V_2O_5 sample (900N010) (a) SEM micrograph (b) at the ZnO grain (c) at the ZnO grain boundary showing V segregation in it and (d) at the triplet point.

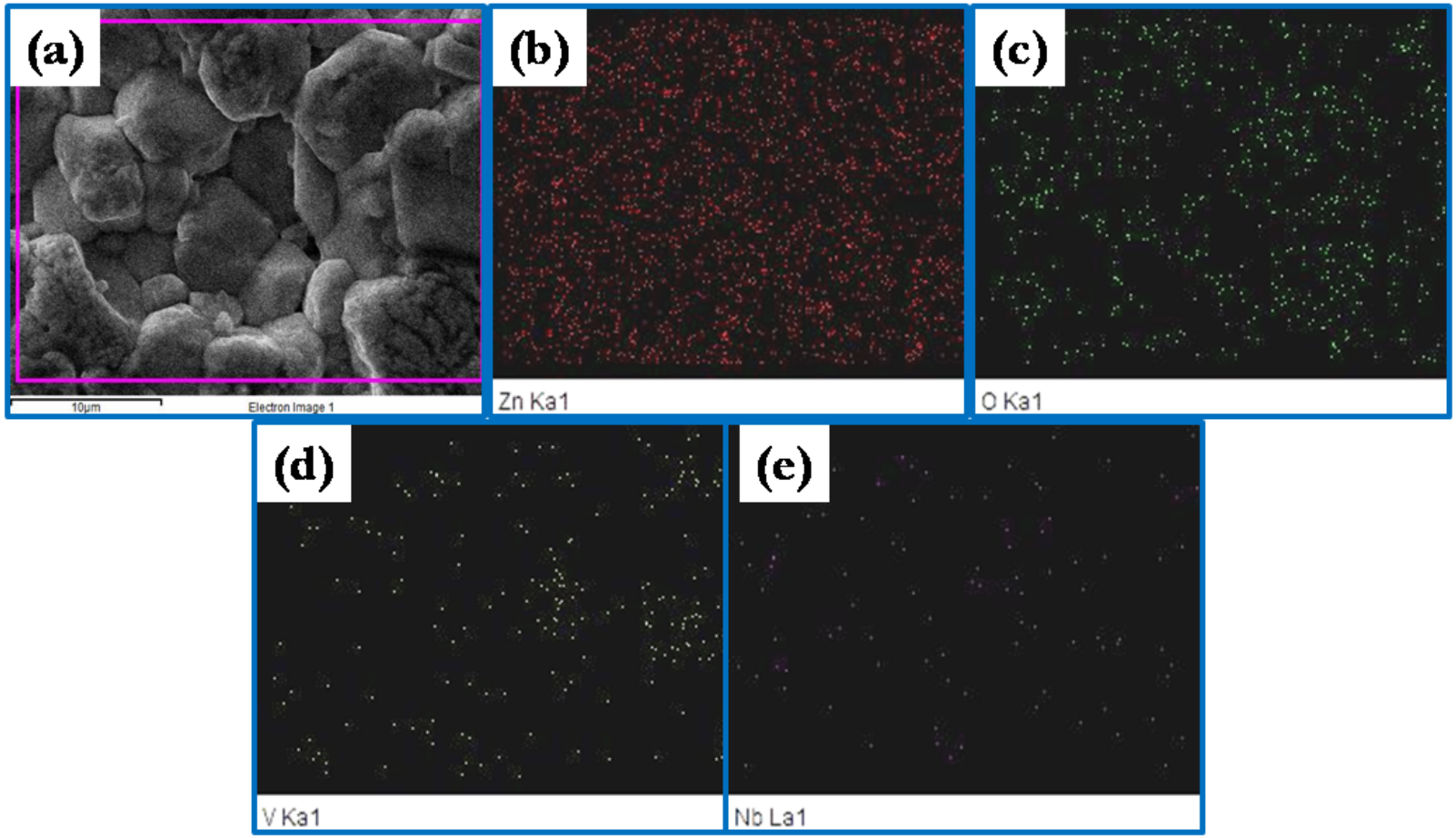

Figure 5.12: EDS elemental maps for 0.10 mol% Nb doped ZnO-V_2O_5 sample (900N010) (a) SEM micrograph (b) Zn map (c) O map (d) V map and (e) Nb map.

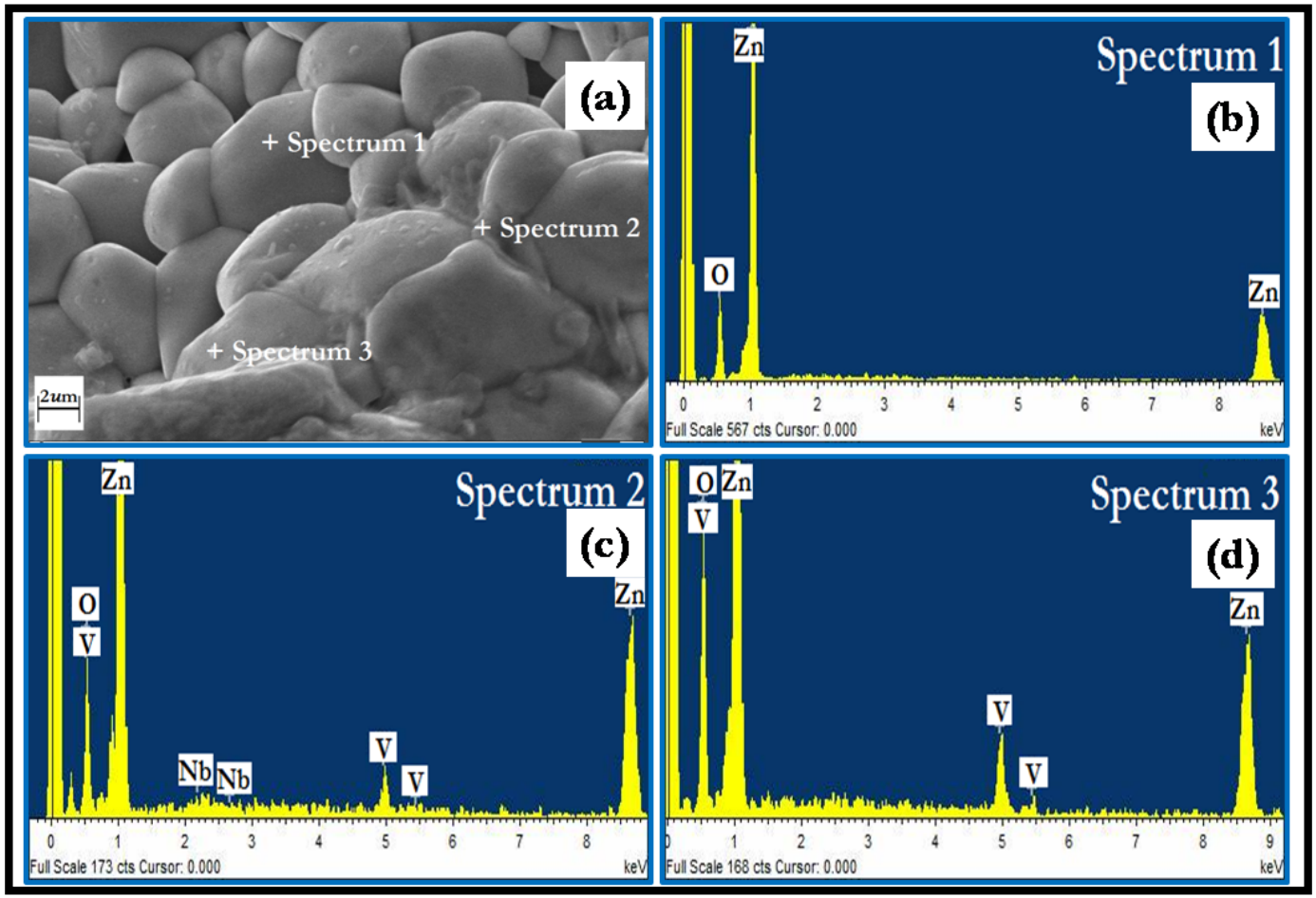

Figure 5.13: EDS spectra 0.50 mol% Nb doped ZnO-sample (900N050) (a) SEM micrograph (b) at the ZnO grain (c) at the ZnO grain boundary showing V segregation in it and (d) at the bubble/dot on ZnO grain.

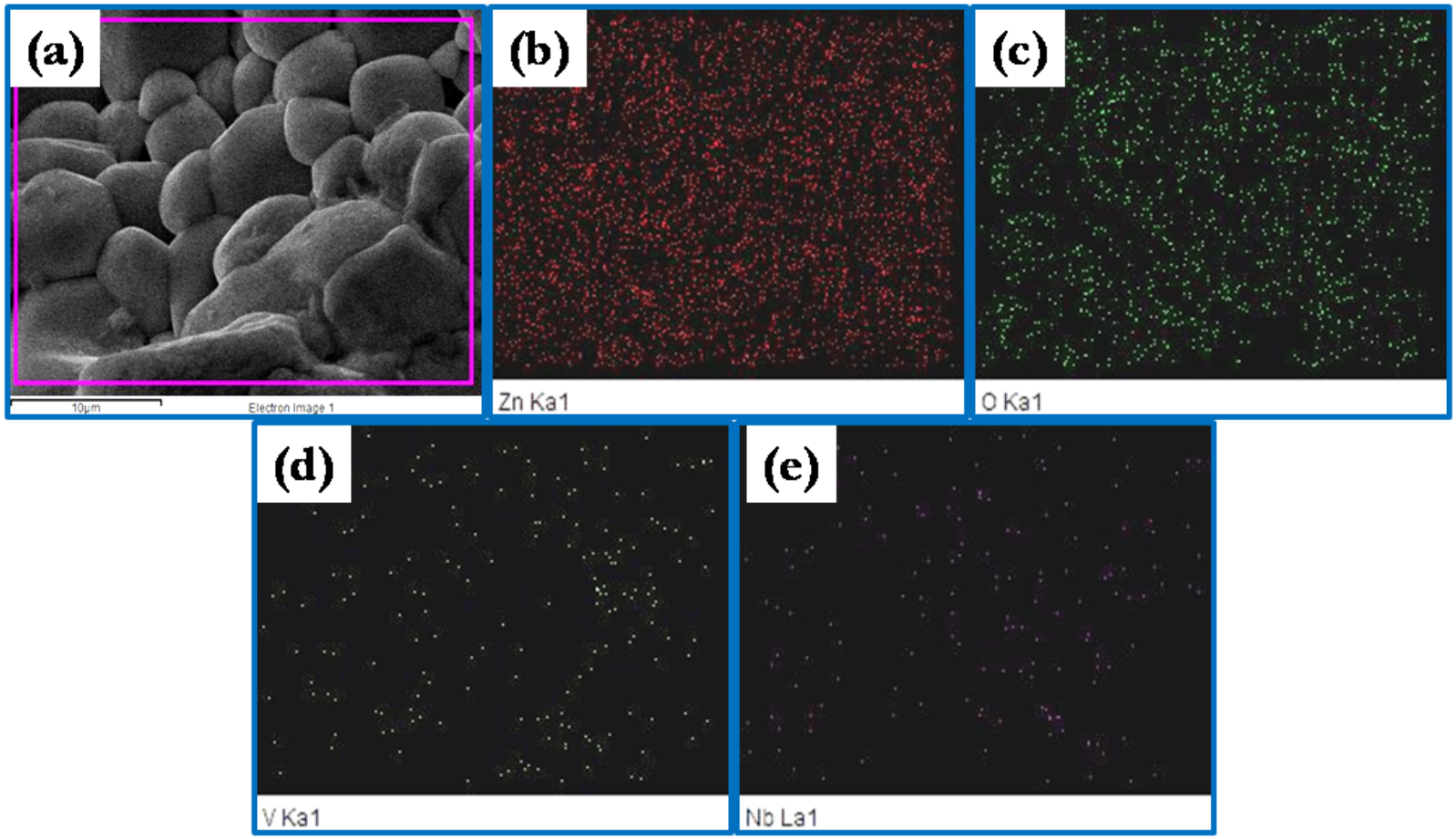

Figure 5.14: EDS elemental maps for 0.50 mol% Nb doped ZnO-V_2O_5 System (900N050) (a) SEM micrograph (b) Zn map (c) O map (d) V map and (e) Nb map.

5.1.4. Percentage Theoretical Density

Fig. 5.15(a) shows the plot between percentage theoretical density vs. mol% Nb_2O_5 for the samples sintered at 850˚C.

The sintered density of the samples sintered at 850 ˚C was found to be in the range approximately 5.30-5.33 gm/cc given in Table 5.1, corresponding to 90.36 - 93.54 % of the theoretical density (TD). Table 5.4 shows the percentage theoretical density for 0.00, 0.05, 0.10, 0.25 and 0.50 mol% Nb_2O_5 doped ZnO-V_2O_5 samples are 90.36, 92.42, 93.54, 93.44 and 93.26 % respectively. Percentage theoretical density increases with the Nb_2O_5 doping to 0.10 mol%, further addition decreases the percentage theoretical density.

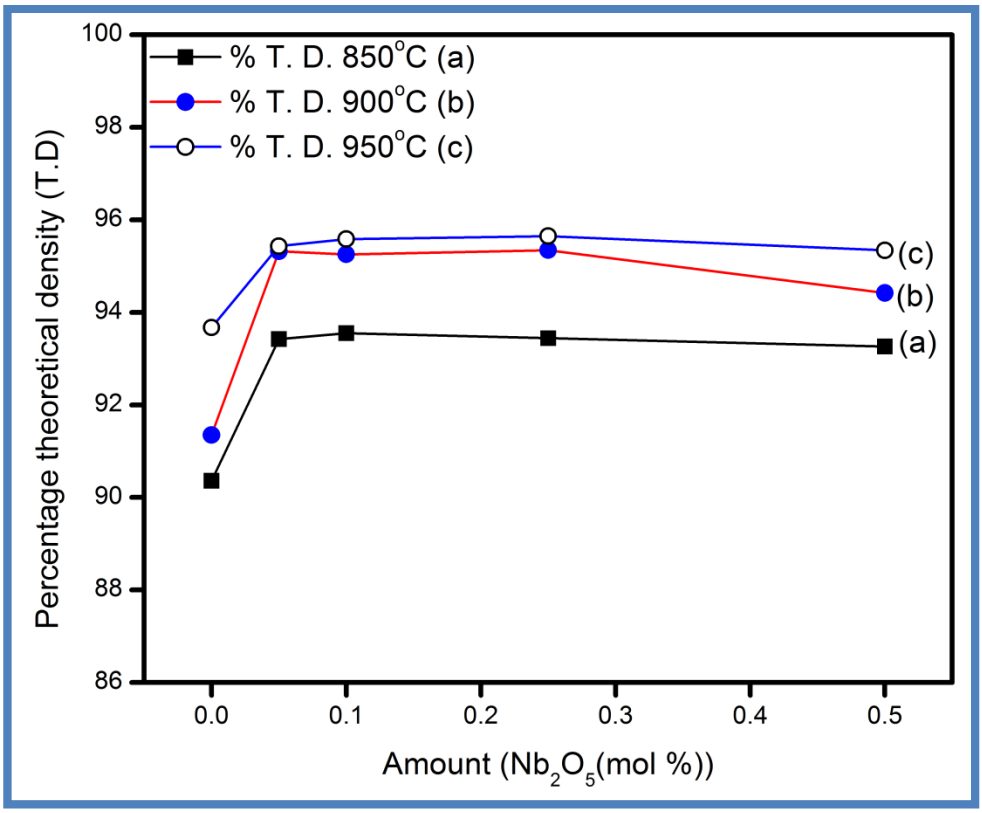

Fig. 5.15 shows the plot of percentage theoretical density vs. mol% Nb_2O_5 for the samples sintered at (a) 850 ˚C; (b) 900 °C and (c) 950 °C.

Fig. 5.15(b) shows the plot between percentage theoretical density vs. mol% Nb_2O_5 for the samples sintered at 900˚C. The sintered density of the samples sintered at 900˚C was found to be in the range approximately 5.37 - 5.49 gm/cc given in Table 5.2, corresponding to 91.35 – 95.34 % of the theoretical density (TD). Sample 900N000 shows the high value of density (5.49 gm/cc). Table 5.5 shows the percentage theoretical density for 0.00, 0.05, 0.10, 0.25 and 0.50 mol% Nb_2O_5 doped ZnO-V_2O_5 samples are 91.35, 95.32, 95.25, 95.34 and 94.42 % respectively.

Fig. 5.15(c) shows the plot between percentage theoretical density vs. mol% Nb_2O_5 for the samples sintered at 950˚C. The sintered density of the samples sintered at 950˚C was found to be in the range approximately 5.411-5.483 gm/cc given in Table 5.3, corresponding to 93.67 - 95.65 % of the theoretical density (TD). Sample 900N000 shows the high value of density (5.48 gm/cc). Table 5.5 shows the percentage theoretical density for 0.00, 0.05, 0.10, 0.25 and 0.50 mol% Nb_2O_5 doped ZnO-V_2O_5 samples are 93.67, 95.33, 95.58, 95.65 and 95.34 % respectively. It was assumed that the decrease of the sintered density is ascribed to the volatility of the V-species for V_2O_5 with a low melting point.

Addition of Nb as well as sintering temperature increases percentage theoretical density. The ZnO has a eutectic reaction with $Zn_3(VO_4)_2$ at 890˚C and for sintering at ≥ 900˚C, it has been suggested that the liquid phase of $Zn_3(VO_4)_2$ enhance densification by solution and reprecipitation of ZnO.

5.2. Electrical Behavior of Nb_2O_5 Doped ZnO–V_2O_5 Varistor.

5.2.1. Non-Linear Properties

The varistor properties are featured by the conduction characteristics, which do not follow Ohm's law in the E–J relation. Basically, the curves are divided into two regions: one is a linear insulating region with high resistance before breakdown field and other is a nonlinear conducting region with low resistance after the breakdown field. The sharp knee of the curves leads to the better varistor properties.The behaviour of E_{1mA} in accordance with Nb_2O_5 content can be explained by the following expression:

$$E_{1mA} = V_{gb}/d, \quad (5.1)$$

where d is the grain size, and V_{gb} is the breakdown voltage per grain boundary. This expression indicates that the V_{gb} value is directly determined from E_{1mA} [Levinson et al. (1975)].

Fig. 5.16 shows the electric field–current density (E–J) characteristics of the samples sintered at 850 °C. The breakdown field (E_{1mA}) increased from 95 to 353 V/mm and then decreased to 282 V/mm with the further increase of the Nb content. Therefore, the decrease of E_{1mA} with the increase of the Nb content is attributed to the decrease of the breakdown voltage per grain boundary and the increase of the average ZnO grain size.

The leakage current density decreased from 556.8 to 372.5 μA/cm^2 with increased content of Nb. However, further increase in the Nb content caused J_L to increase to 424.8 μA/cm^2, as shown in Fig. 5.16. The decrease of J_L is attributed to the increase of the minority carriers in the grain boundary. The nonlinear coefficient (α) was increased from 2.7 to 4.5 with the increasing content of Nb. However, further increase caused α to decrease upto 3.6, as shown in Fig. 5.17. As a result, it can be seen that the Nb content has a significant effect on the nonlinear properties of these ceramics in light of a variation. The E–J characteristic parameters are summarized in Table 5.7 and shown in Fig. 5.17. The reduction in the number of grain boundaries per unit thickness due to grain enlargement should have caused of decrease in α value.

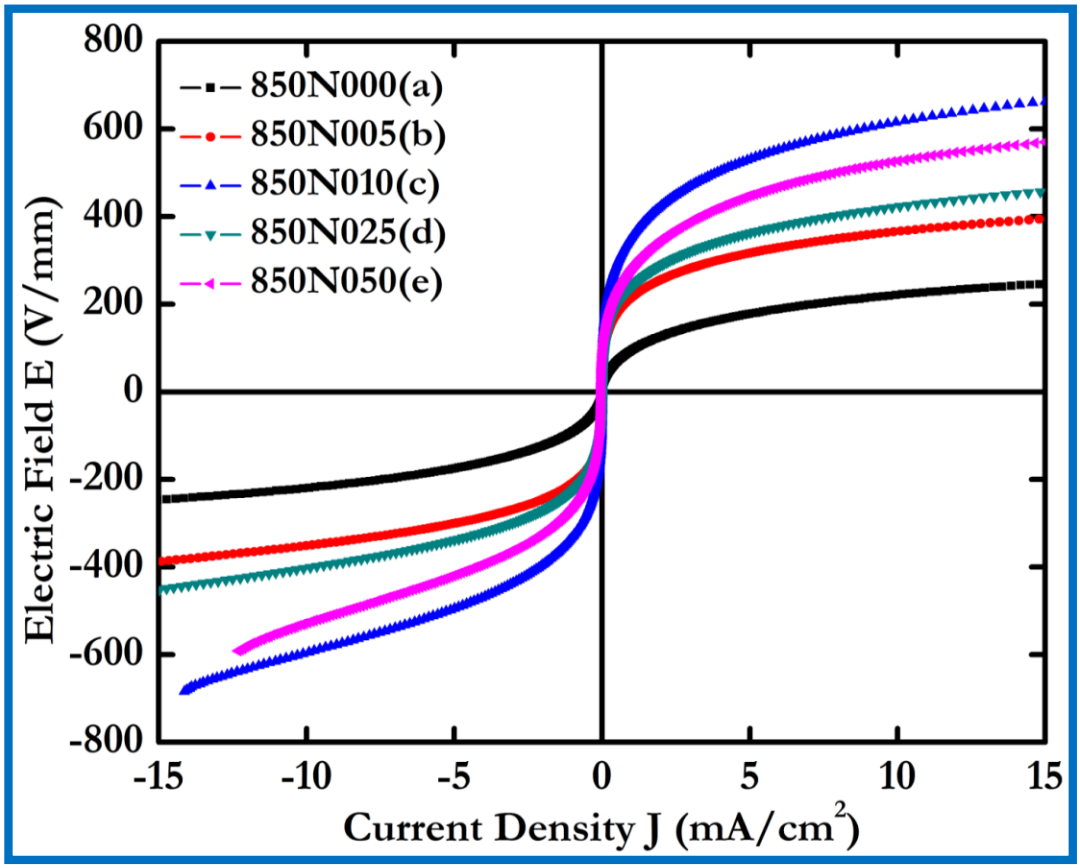

Figure 5.16: E-J curve showing the effects of Nb_2O_5 content in ZnO-V_2O_5 materials sintered at 850 °C: (a) 850N000 (0.00 mol% Nb); (b) 850N005 (0.05 mol% Nb); (c) 850N010 (0.10 mol% Nb); (d) 850N025 (0.25 mol% Nb) and (e) 850N050 (0.50 mol% Nb).

Table 5.7: Summary of electrical results obtained for Nb_2O_5 doped ZnO-V_2O_5 materials sintered at 850 °C

Sample name	Alpha (α)	Breakdown field (V/mm)	Leakage current density J_L (μA/cm²)	Vgb (V/gb)	ε' (1kHz)	Tan δ (1kHz)
850N000	2.7	95.4	556.8	0.56	1381	0.338
850N005	4.3	216	359.9	1.11	674	0.266
850N010	4.5	353	372.5	1.85	519	0.188
850N025	4.0	240	390.7	1.24	739	0.293
850N050	3.6	282	424.8	1.43	809	0.343

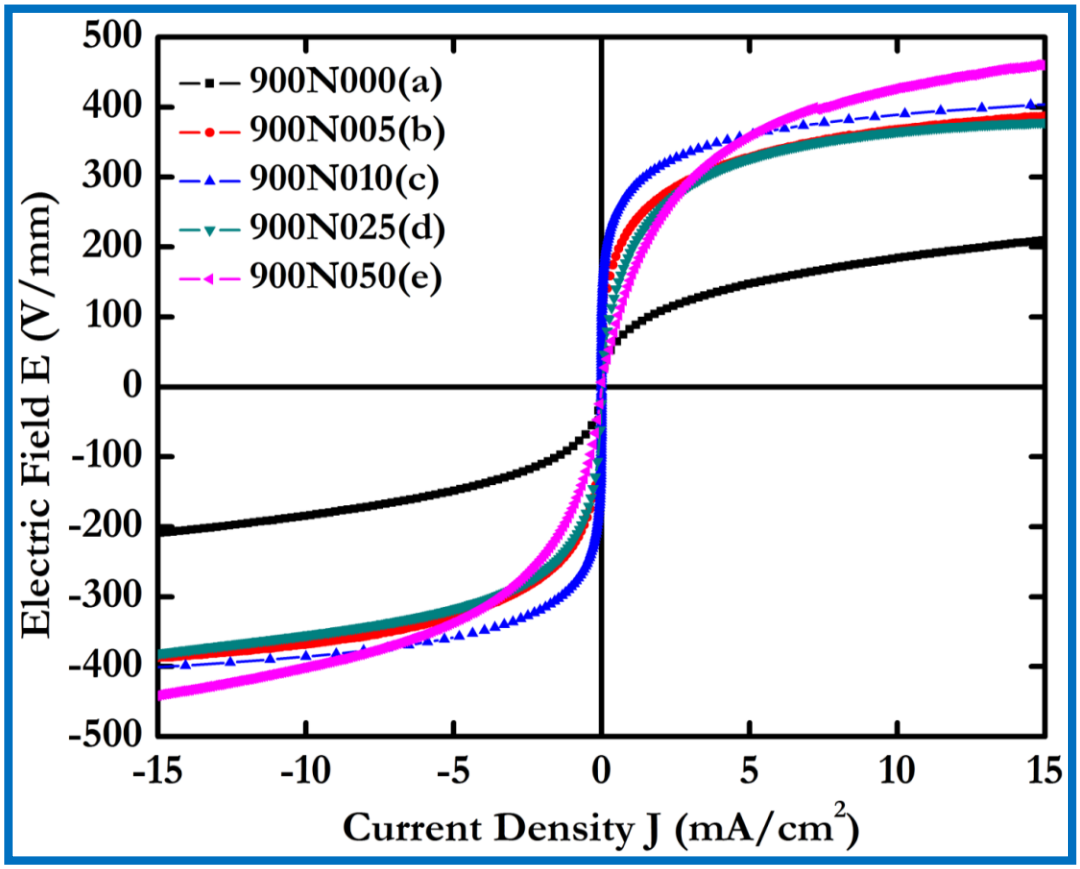

Figure 5.17: E-J curve showing the effects of Nb_2O_5 content in ZnO-V_2O_5 material sintered at 900°C: (a) 900N000 (0.00 mol% Nb); (b) 900N005 (0.05 mol% Nb); (c) 900N010 (0.10 mol% Nb); (d) 900N025 (0.25 mol% Nb) and (e) 900N050 (0.50 mol% Nb).

Table 5.8: Summary of electrical results obtained for Nb_2O_5 doped ZnO-V_2O_5-materials sintered at 900 °C

Sample name	Alpha (α)	Breakdown field (V/mm)	Leakage current density J_L (μA/cm2)	V_{gb} (V/gb)	ε' (1kHz)	Tan δ (1kHz)
900N000	2.9	83	580.6	0.70	2123	0.234
900N005	4.9	229	461.5	1.33	545	0.081
900N010	7.1	281	310.6	1.98	719	0.079
900N025	3.7	195	621.6	1.43	618	0.115
900N050	2.3	157	748.5	1.72	389	0.171

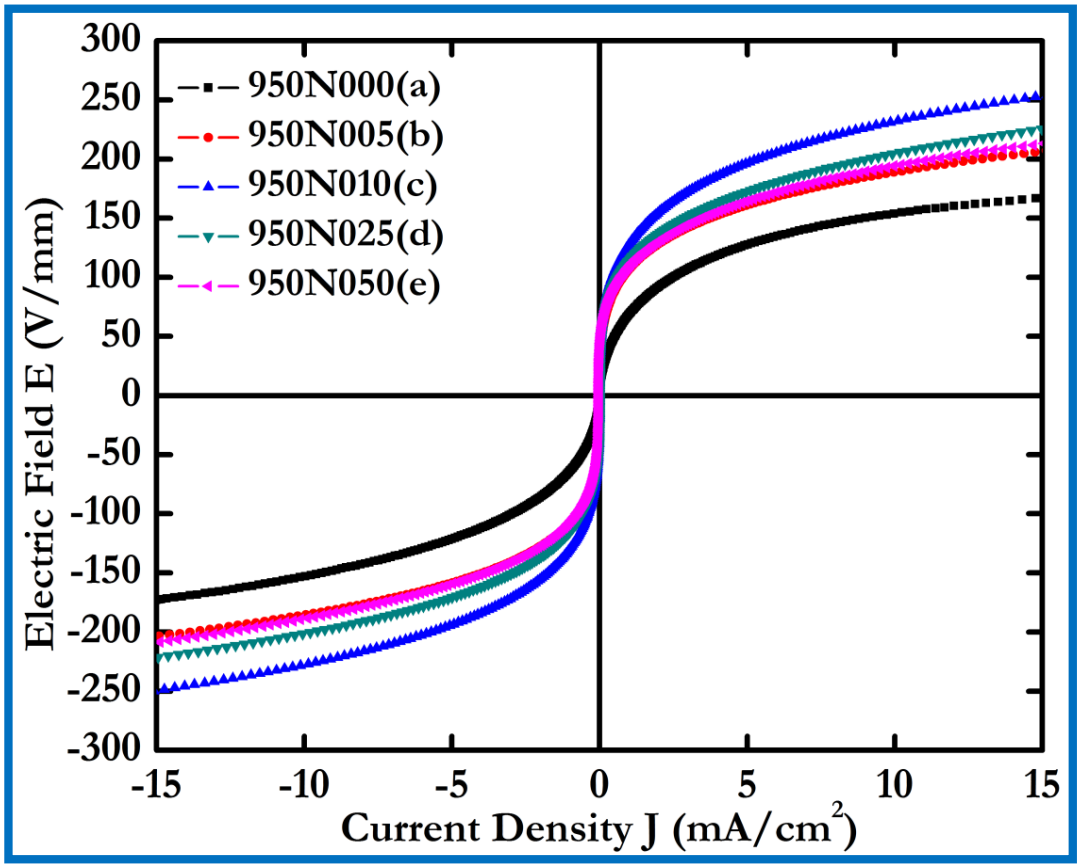

Figure 5.18: E-J curve showing the effects of Nb_2O_5 content in ZnO-V_2O_5 materials sintered at 950 °C: (a) 950N000 (0.00 mol% Nb); (b) 950N005 (0.05 mol% Nb); (c) 950N010 (0.10 mol% Nb); (d) 950N025 (0.25 mol% Nb) and (e) 950N050 (0.50 mol% Nb).

Table 5.9: Summary of electrical results obtained for Nb_2O_5 doped ZnO-V_2O_5 materials sintered at 950 °C

Sample name	Alpha α	Breakdown field (V/mm)	Leakage current density J_L (μA/cm²)	V_{gb} (V/gb)	ε' (1kHz)	Tan δ (1kHz)
950N000	2.8	69	540.6	1.15	3063	0.304
950N005	4.0	106	366.7	1.45	1274	0.204
950N010	4.1	128	385.8	1.92	928	0.189
950N025	3.9	115	351.4	1.70	925	0.172
950N050	3.8	110	388.3	1.71	1076	0.286

Fig. 5.17 shows the electric field–current density (E–J) characteristics of the samples sintered at 900 °C. The breakdown field (E_{1mA}) increased from 83 to 281 V/mm and then decreased to 156 V/mm with the increase of the Nb content. Therefore, the decrease of E_{1mA} with the increasing content of Nb is attributed to the decrease of the breakdown voltage per grain boundary and the increase of the average ZnO grain size. The leakage current density decreased from 580.6 to 310.6 μA/cm^2 with increasing content of Nb.

However, further increasing Nb content caused J_L to increase 748.5 μA/cm^2, as shown in Fig. 5.17. The decrease of J_L is attributed to the increase of the minority carriersinthe grain boundary. The nonlinear coefficient (α) was increased from 2.9 to 7.1 with the increase in the Nb content. However, further increase caused decrease of α to 2.3, as shown in Fig. 5.18. As a result, it can be seen that the Nb content has a significant effect on the nonlinear properties of these ceramics in light of a variation. The E–J characteristic parameters are summarized in Table 5.8 and shown in Fig. 5.17. The reduction in the number of grain boundaries per unit thickness due to grain enlargement should have caused a decrease in α value.

Fig. 5.18 shows the electric field–current density (E–J) characteristics of the samples sintered at 950 °C. The breakdown field (E_{1mA}) increased from 69 to 128 V/mm and then decreased to 110 V/mm with the increasing in content of Nb. The decrease of E_{1mA} with the increase of the Nb content is attributed to the decrease of the breakdown voltage per grain boundary and the increase of the average ZnO grain size. The leakage current density decreased from 540.6 to 385.8 μA/cm^2 with an increase in the Nb content. However, further increase in the Nb content caused J_L to increase to 388.3 μA/cm^2, as shown in Fig. 5.18. The decrease of J_L is attributed to the increase of the minority carriers in the grain boundary.

The nonlinear coefficient (α) was increased from 2.8 to 4.1 with the increasing Nb content. However, a further increase caused decrease of α to 3.8, as shown in Fig. 5.18. As a result, it can be seen that the Nb content has a significant effect on the nonlinear properties of these ceramics in light of a variation. The E–J

characteristic parameters are summarized in Table 5.9 and shown in Fig. 5.18. The reduction in the number of grain boundaries per unit thickness due to grain enlargement should have caused to decrease in α value.

This suggests that segregation of Nb in the grain boundary promoted the development of the essential potential barrier at the interface. Adversely, excessive Nb doping encourage thicker grain bondary formation that could lead to poor non-linearity and lower bulk resistance. The behaviour of α in accordance with the Nb content can be related to the variation of the schottky barrier height according to the variation of the electronic states at the grain boundaries.

5.2.2. Dielectric Spectroscopy

Fig. 5.19 shows the dielectric characteristics of the samples sintered at 850 °C with different doping of Nb_2O_5.The ε' and tan δ at 1kHz for the 0.00, 0.05, 0.10, 0.25 and 0.50 mol% Nb_2O_5 doped ZnO-V_2O_5 samples sintered at 850 °C are 1381, 673, 519, 739, 808 and 0.338, 0.266, 0.189, 0.293, 0.343 respectively. At lower frequencies, a high relative dielectric permittivity was found. The dispersion of the dielectric properties is obvious. The formation of the grain boundary barrier layer was also confirmed by the rapid decrease of the apparent dielectric constant with increasing frequency of the ceramics and the non-ohmic I-V behaviour.

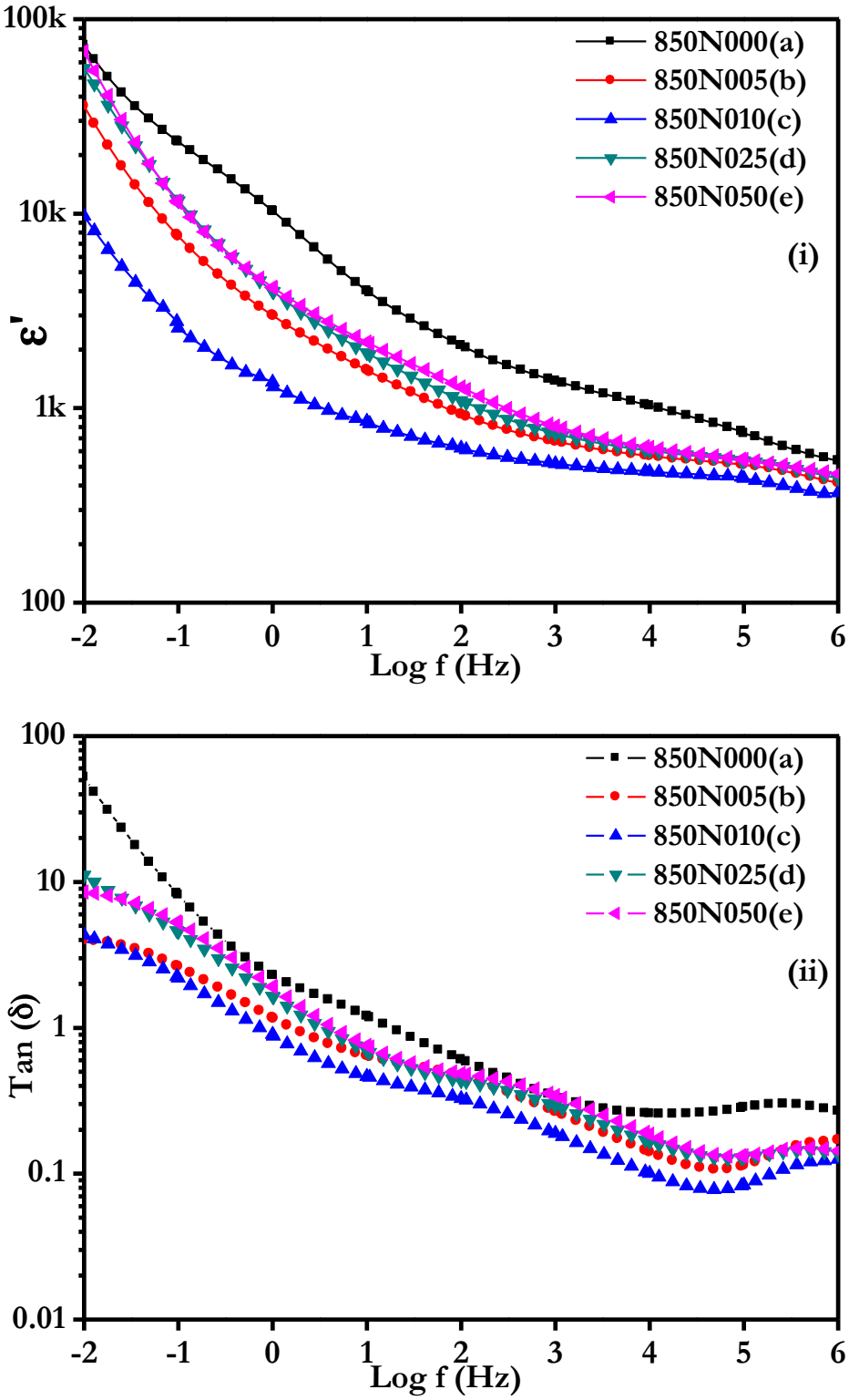

Figure 5.19: Plot of (i) έ and (ii) tan δ vs frequencey of varying Nb_2O_5 doping in $ZnO\text{-}V_2O_5$ materials sintered at 850 °C.

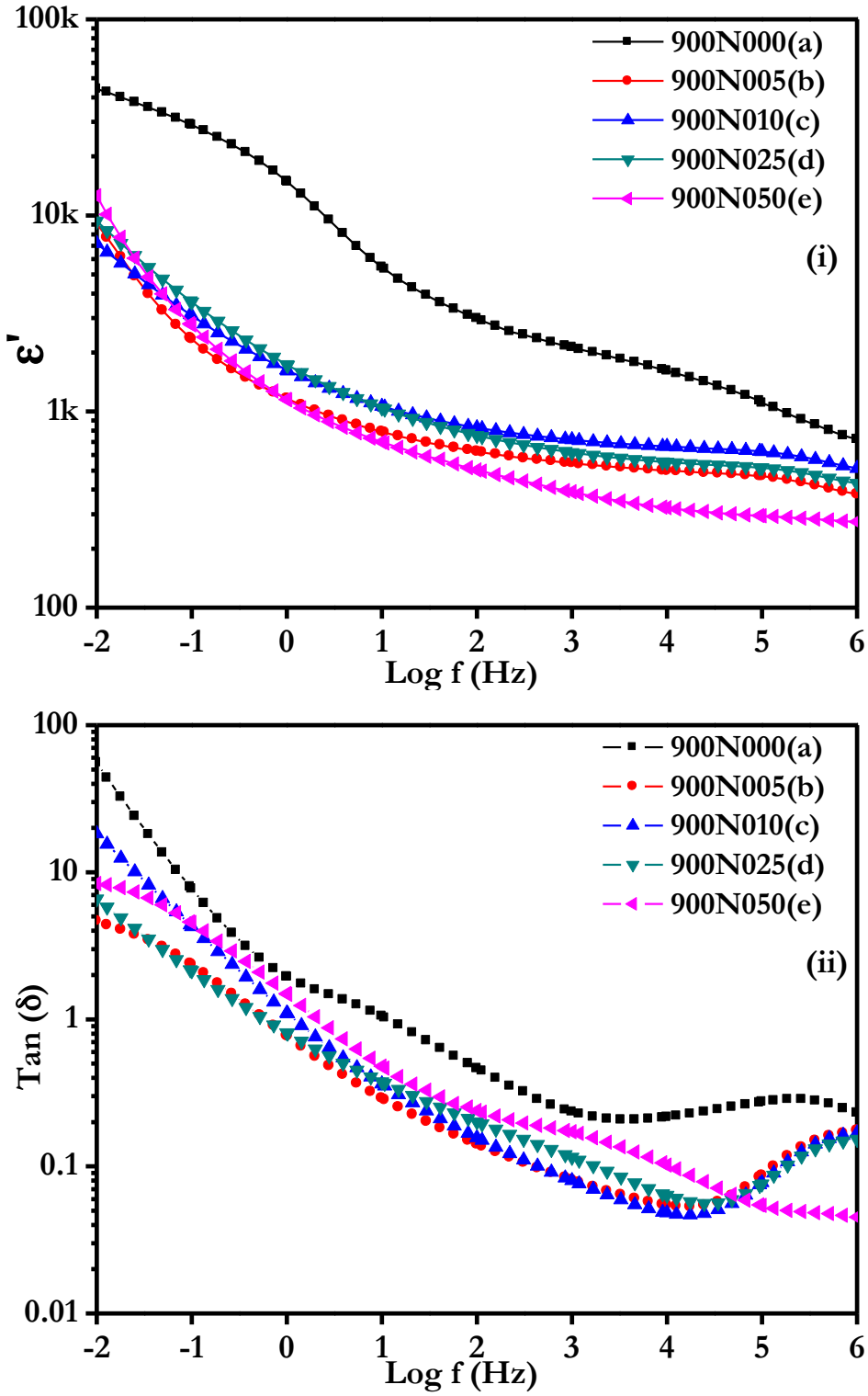

Figure 5.20: Plot of (i) έ and (ii) tan δ vs frequencey of varying Nb_2O_5 content in ZnO-V_2O_5 materials sintered at 900 °C.

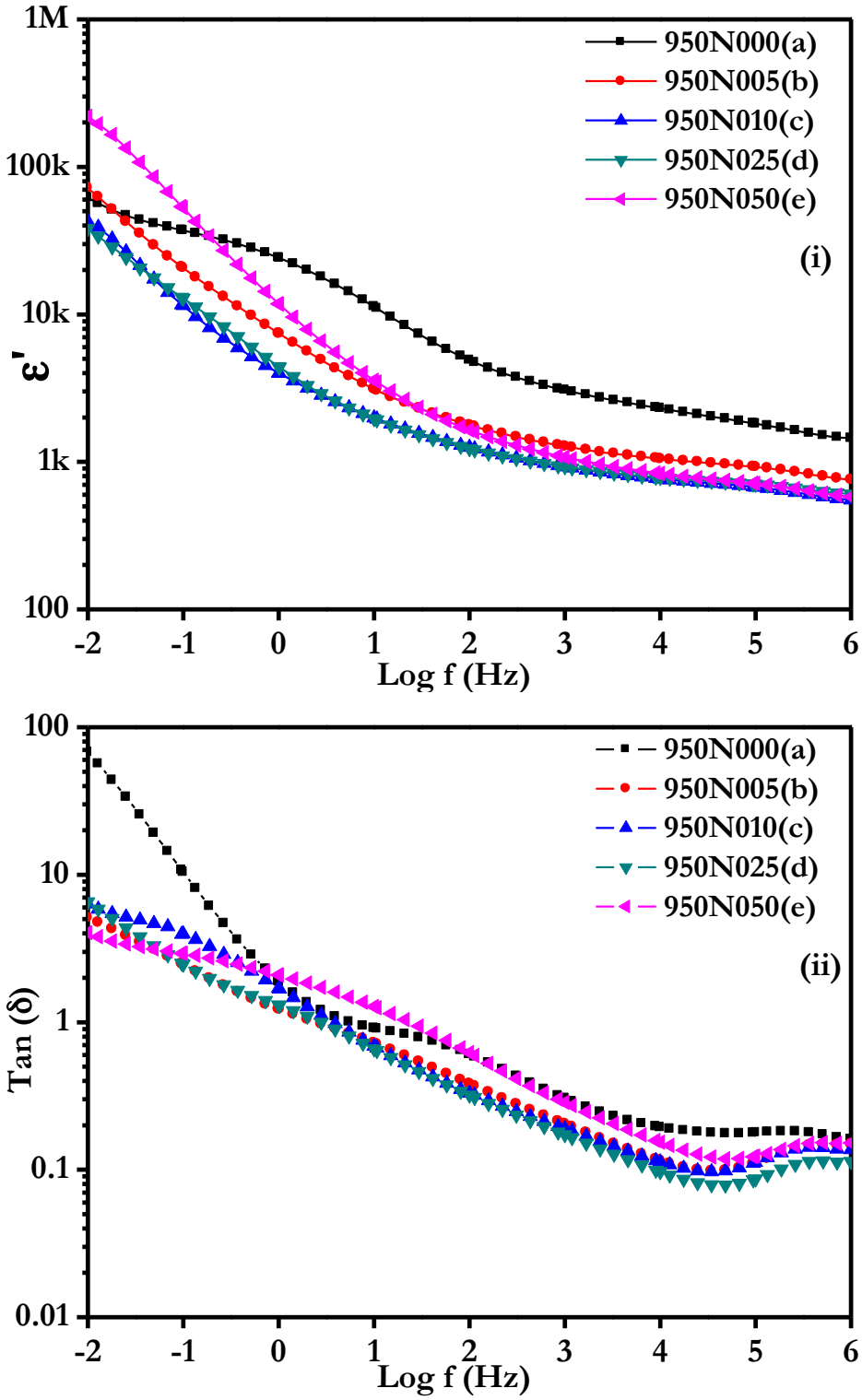

Figure 5.21: Plot of (i) έ and (ii) tan δ vs frequencey of varying Nb_2O_5 content in ZnO-V_2O_5 materials sintered at 950 °C.

Fig. 5.20 shows the dielectric characteristics of the samples sintered at 900 °C with different dopings of Nb_2O_5.The ε' and tan δ at 1kHz for the 0.00, 0.05, 0.10, 0.25 and 0.50 mol% Nb_2O_5 doped ZnO-V_2O_5 samples sintered at 900 °C are 2123, 545, 719, 618, 389 and 0.234, 0.081, 0.079, 0.115, 0.171 respectively. Heterogeneities in the grains and/or the presence of the potential barriers between the grains are responsible for the similar dielectric properties in a number of materials. Orientational polarization (zinc interstitials and oxygen vacancies) is dominant at higher frequencies, whereas the high degree of dispersion observed at the low-frequency region is attributable to interfacial polarization.

Fig. 5.21 shows the dielectric characteristics of the samples sintered at 950 °C with different doping of Nb_2O_5. The ε' and tan δ at 1kHz for the 0.00, 0.05, 0.10, 0.25 and 0.50 mol% Nb_2O_5 doped ZnO-V_2O_5 samples sintered at 950 °C 3063, 1274, 928, 925, 1076 and 0.304, 0.204, 0.189, 0.172, 0.286 respectively.

As the doping of Nb_2O_5 increases, the dielectric constant (ε') decreases with less sharp dispersive drop with increasing frequency, which is closely associated with the polarization of dielectrics. It is assumed that this is attributed to the decrease of the number of dipole, which can follow the test frequency. It is observed that the ε' measuring within the frequency range depends on the doping of Nb_2O_5. This is directly related to the average grain size and depletion layer width, as can be seen in the following expression:

$$\varepsilon' = \mathcal{E}_g \frac{d}{t} \tag{5.2}$$

where ε' is the dielectric constant of ZnO (8.5), d is the average grain size, and t is the depletion layer width of the both sides at the grain boundaries. The decrease of d/t ratio in above equation gives rise to the decrease of the ε'. For the Samples sintered at 900 °C, the ε' at 1 kHz decreased from 2123 to 389. On the other hand, the tan δ decreased until the vicinity of 10 kHz with the increasing frequency. This exhibits weak absorption peak in the vicinity of 30-50 kHz. The detailed dielectric parameters are summarized in Tables from 5.7 to 5.9.

5.2.3. Impedance Spectroscopy

The semicircle curves observed from Figs. 5.22 to 5.30 (a-e). It was analysed by convolution of two time constant in the system. Thus, the equivalent circuit containing two parallel resistance-constant phase element (CPE) sub-circuits in series was used for fitting the impedance spectra which is shown from Figs. 5.22 to 5.30 (f).

Use of a simple capacitor is not adequate to model the electrical response of the material due to the microstructural heterogeneities of the sample. The appearance of full and partial semicircles or no semicircle depends upon the strength of relaxation and the available frequency range [Bueno et al. (1998); Pattanayak et al. (2014); Choudhary et al. (2013); West et al. (1997)], although these semicircles are depressed. This behaviour manifests that there is a distribution of relaxation times instead of a single relaxation time in the material and confirms the presence of a non-debye type relaxation in the materials. In most real cases related to ceramic materials, the Nyquist plot is depressed, with its centre below the real axis. A perfect semicircle with its centre on the Z'-axis is observed for ideal debye-type relaxation. However, in the studied material, we did not find such debye-type relaxation [Tsai (1994); (1996)]. A constant phase element (CPE) is used to represent the non-ideal debye type behaviour, which has impedance given by Abram et al. [2003], and is introduced with the resistors and capacitors or a CPE. The CPE is equivalent to a distribution of capacitors in parallel. The impedance function of the CPE element is

$$Z_{CPE} = \frac{1}{P(j\omega)^n} \tag{5.3}$$

where P is a constant that is independent of frequency, ω = 2πf is the angular frequency (f is the applied frequency in Hz), $j = \sqrt{-1}$ and n is an exponential index, which is measure of arc depression. When constant n = 0, the CPE acts as a pure resistor with value = $1/P$, while n = 1 for ideal debye-like behaviour, in which, the CPE represents an ideal capacitor (C = P). The capacitor is frequency dependent when the n value is below unity. In most real cases of ceramic materials, the arc in complex impedance plots of Im(Z') versus Re (Z") is

depressed, with its centre below the real axis. However, in polycrystalline semiconductor ceramics, the trapping of the charge at grain boundaries appears to have a significant effect on the electrical transport properties due to the formation of electrostatic potential barriers [Abram et al. (2003)].

The electrode contribution to the overall electrolyte resistance has not been considered. Two hypotheses may be considered to explain these two time constants. The first hypothesis suggests that one time constant is related to the grain barrier and the second is associated with the grain boundary barrier. The limitation of this model is that the grain resistivity calculated at 50 °C, 150 °C & 250 °C thus calculated is higher than the literature values reported for grain resistivity of ZnO [West et al. (1997)]. The second hypothesis of the existence of different defects and/or adsorbed species at the grain boundary region, not necessarily at the same grain boundary. The two time constants may be the result of these types of defect. The second hypothesis is more feasible because the possibility of existence of different adsorbed species and defects on ZnO was observed in the literature [Bueno et al. (1998)]. Three regions were apparent. One region appears to be the highly conducting grain cores and was not considered further [West et al. (1997)].The other two regions represent the grain boundary regions that further split into low- and high-frequency regions; these regions were considered further in this work.

To understand the influence of the microstructure and the potential barrier on the electrical properties of ZnO ceramics, the impedance spectra of ZnO pellets were fitted with the electrical equivalent circuits (Figs. 5.22 to 5.30 (f)). The proposed electrical model consists of parallel distributed capacitance represented by resistance R and P (constant phase element). The results of the numerical equivalent circuit parameters fitting of plots using commercially available electrochemical impedance spectroscopy (EIS) [Bondarenko et al. (2005)] for all investigated structures are given in Tables 5.11-5.19.

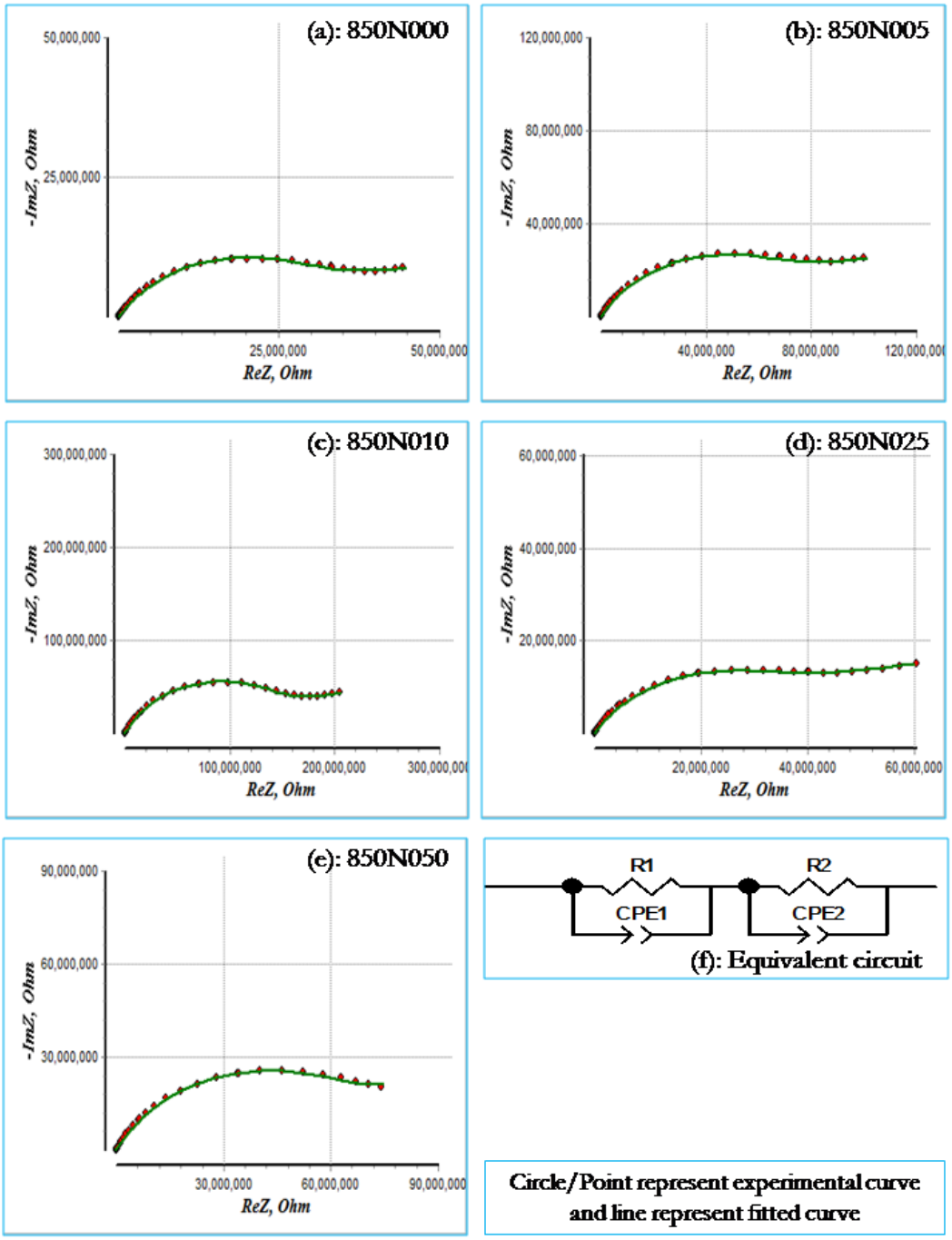

Figure 5.22: Impedance plots for the composition sintered at 850°C and measurement done at 50 °C: (a) 850N000 (0.00 mol% Nb); (b) 850N005 (0.05 mol% Nb); (c) 850N010 (0.10 mol% Nb); (d) 850N025 (0.25 mol% Nb); (e) 850N050 (0.50 mol% Nb) and (f) Equivalent circuit.

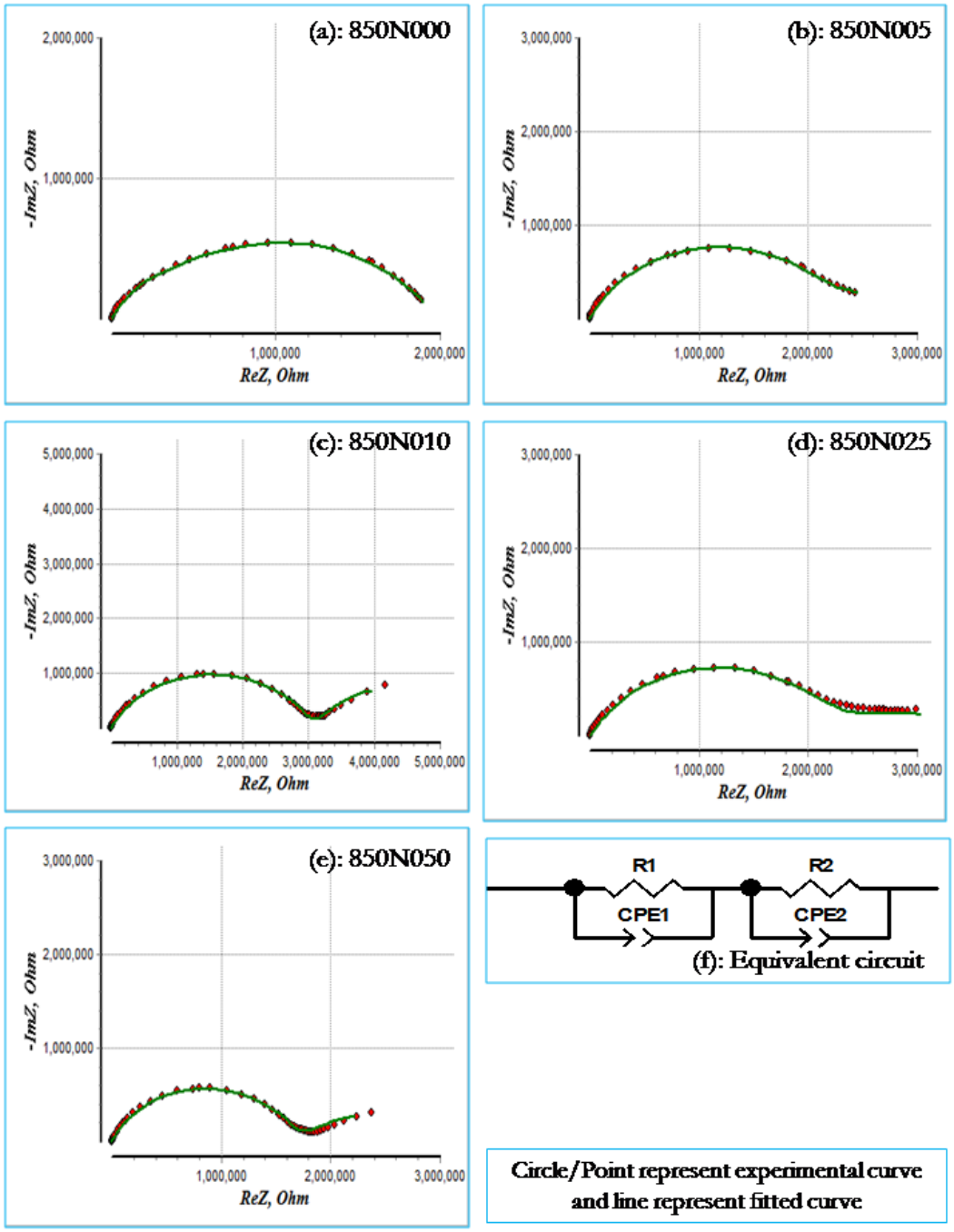

Figure 5.23: Impedance plots for the composition sintered at 850 °C and measurement done at 150 °C: (a) 850N000 (0.00 mol% Nb); (b) 850N005 (0.05 mol% Nb); (c) 850N010 (0.10 mol% Nb); (d) 850N025 (0.25 mol% Nb); (e) 850N050 (0.50 mol% Nb) and (f) Equivalent circuit.

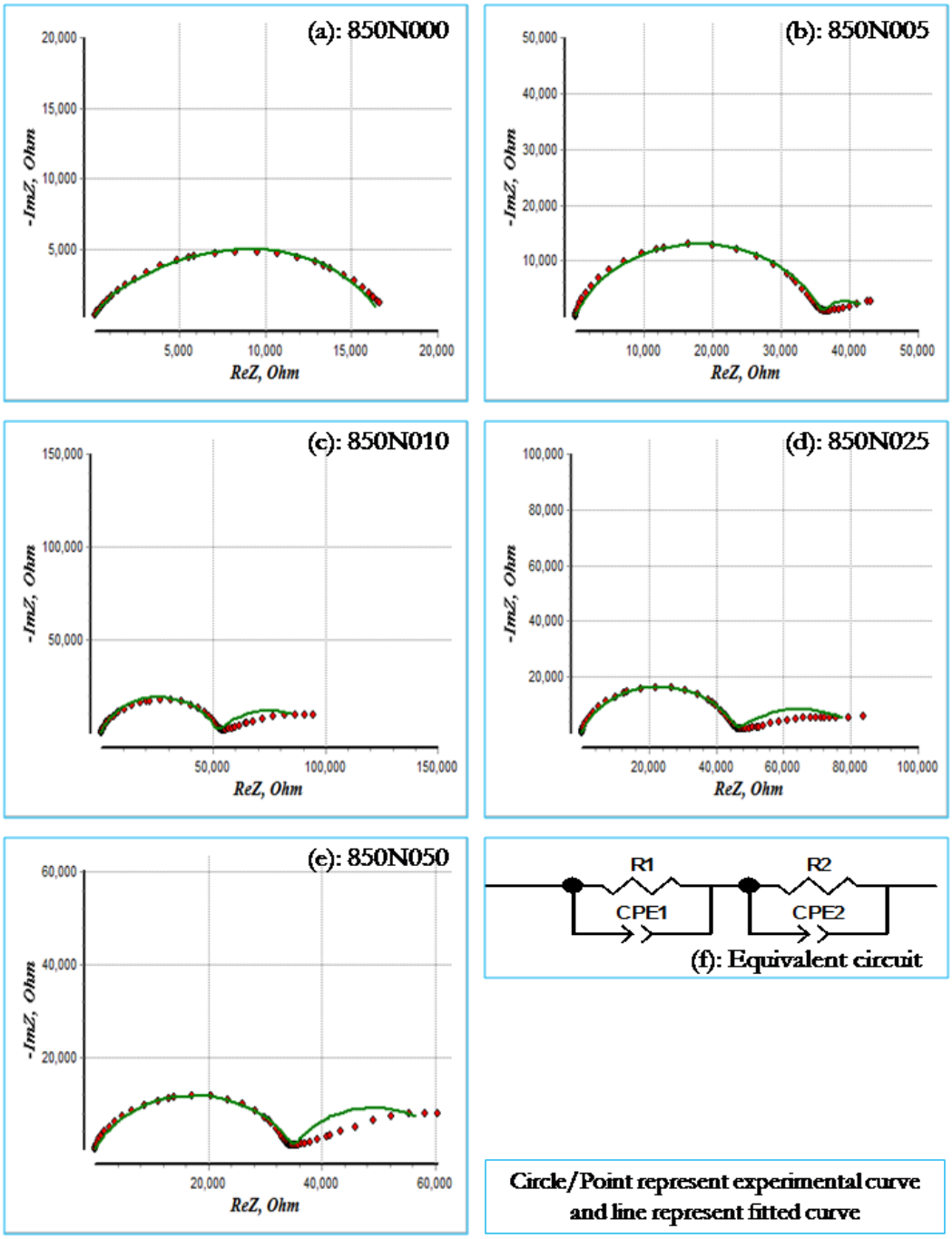

Figure 5.24: Impedance plots for the composition sintered at 850 °C and measurement done at 250 °C: (a) 850N000 (0.00 mol% Nb); (b) 850N005 (0.05 mol% Nb); (c) 850N010 (0.10 mol% Nb); (d) 850N025 (0.25 mol% Nb); (e) 850N050 (0.50 mol% Nb) and (f) Equivalent circuit.

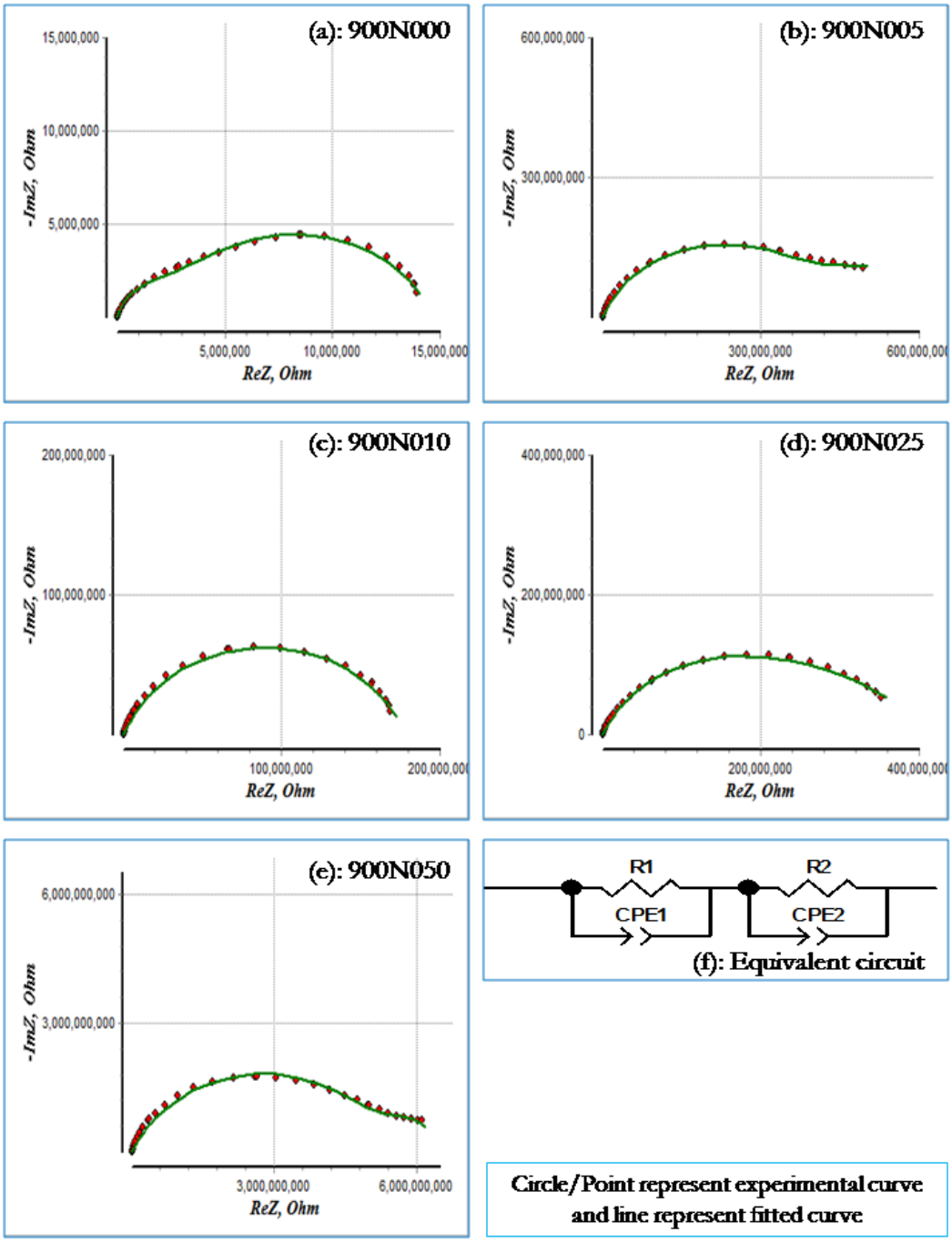

Figure 5.25: Impedance plots for the composition sintered at 900 °C and measurement done at 50 °C: (a) 900N000 (0.00 mol% Nb); (b) 900N005 (0.05 mol% Nb); (c) 900N010 (0.10 mol% Nb); (d) 900N025 (0.25 mol% Nb); (e) 900N050 (0.50 mol% Nb) and (f) Equivalent circuit

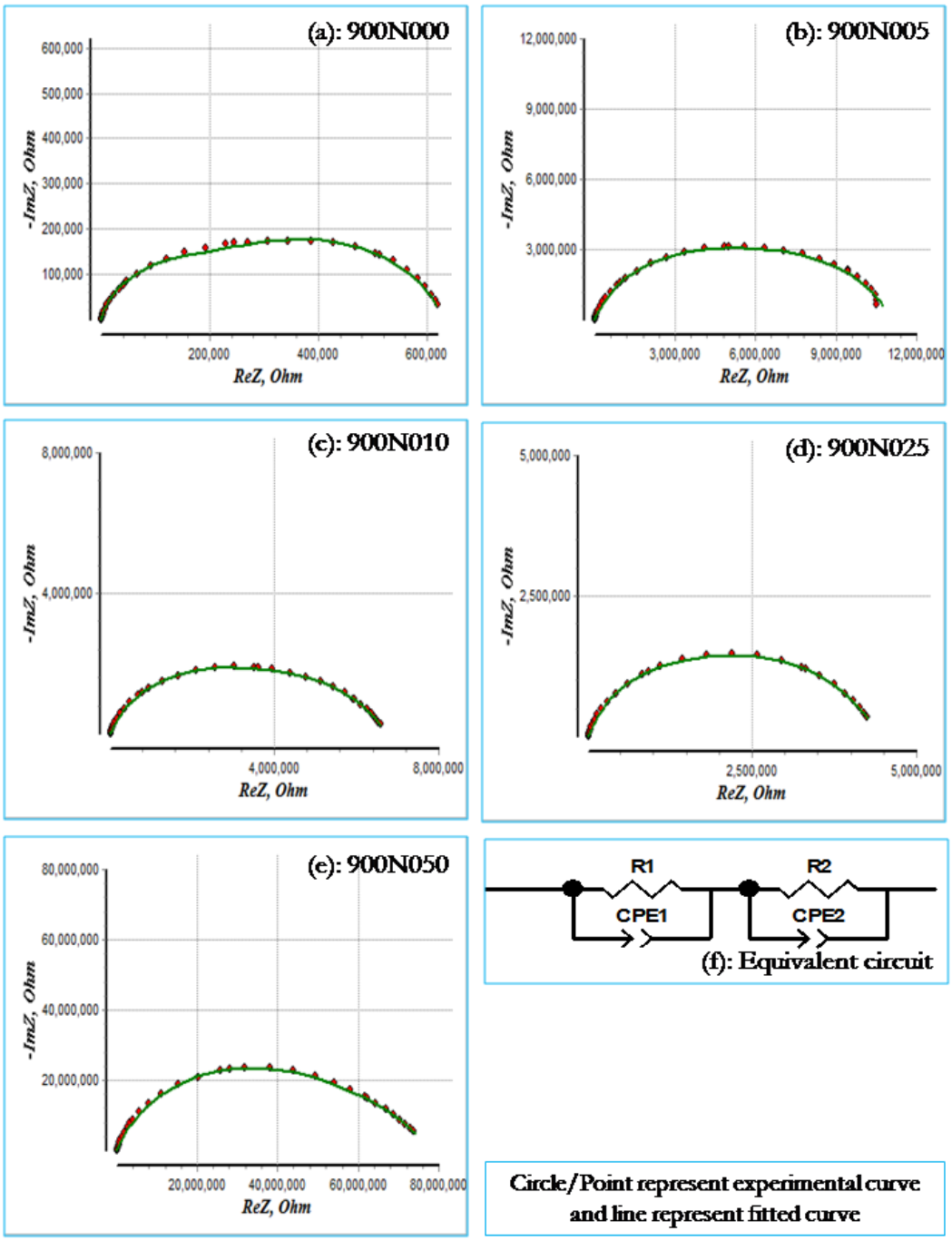

Figure 5.26: Impedance plots for the composition sintered at 900 °C and measurement done at 150 °C: (a) 900N000 (0.00 mol% Nb); (b) 900N005 (0.05 mol% Nb); (c) 900N010 (0.10 mol% Nb); (d) 900N025 (0.25 mol% Nb); (e) 900N050 (0.50 mol% Nb) and (f) Equivalent circuit

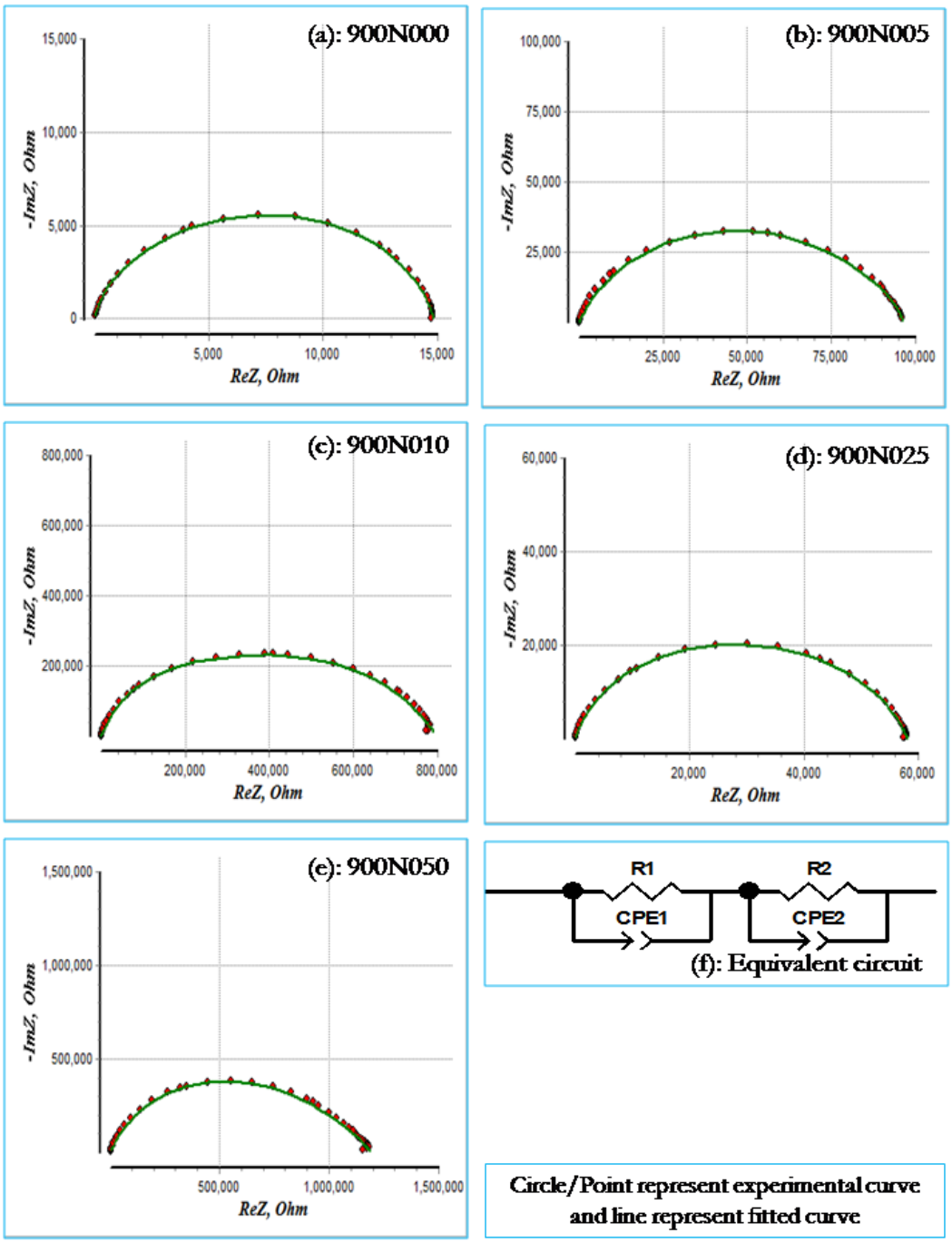

Figure 5.27: Impedance plots for the composition sintered at 900 °C and measurement done at 250 °C: (a) 900N000 (0.00 mol% Nb); (b) 900N005 (0.05 mol% Nb); (c) 900N010 (0.10 mol% Nb); (d) 900N025 (0.25 mol% Nb); (e) 900N050 (0.50 mol% Nb) and (f) Equivalent circuit

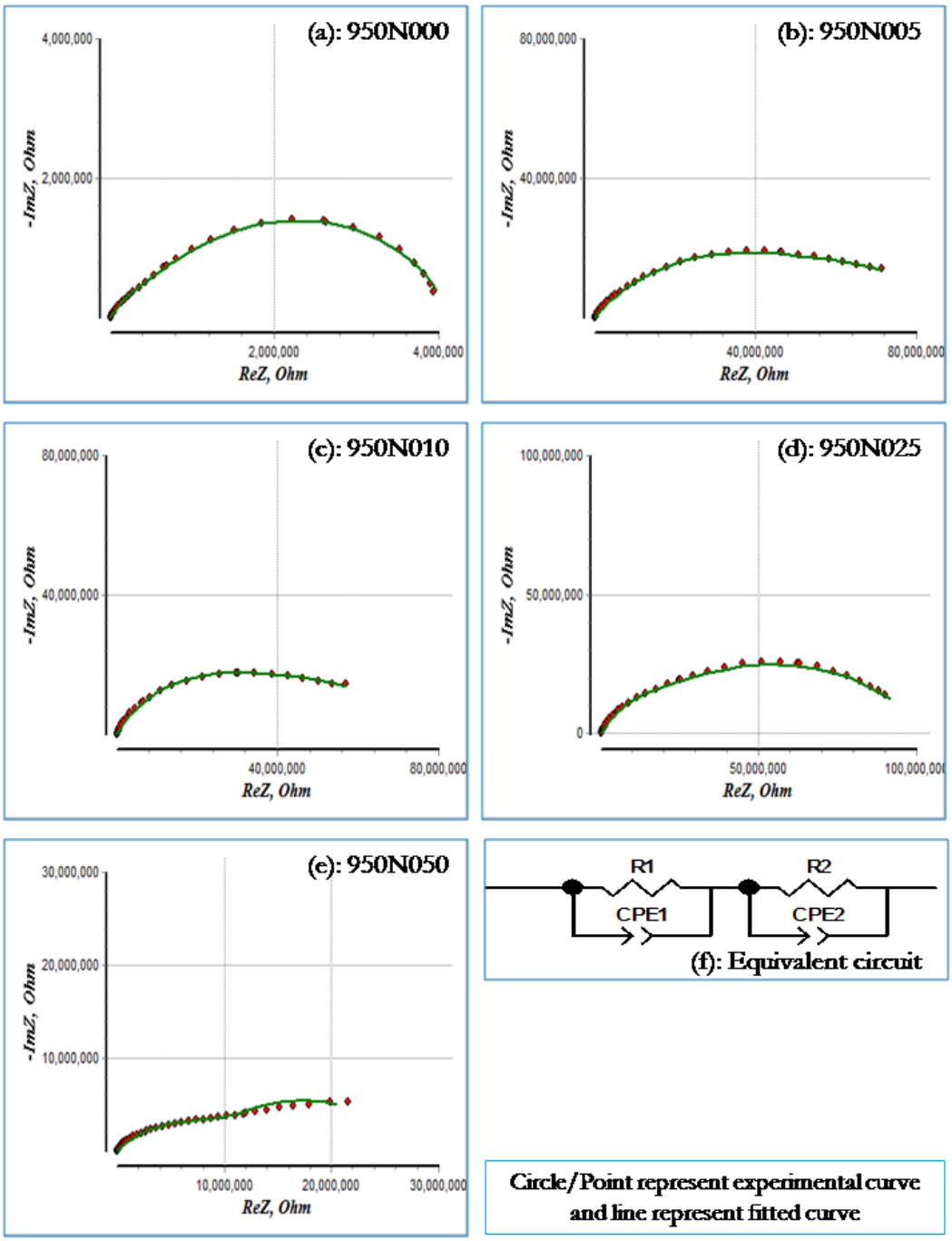

Figure 5.28: Impedance plots for the composition sintered at 950 °C and measurement done at 50 °C: (a) 950N000 (0.00 mol% Nb); (b) 950N005 (0.05 mol% Nb); (c) 950N010 (0.10 mol% Nb); (d) 950N025 (0.25 mol% Nb); (e) 950N050 (0.50 mol% Nb) and (f) Equivalent circuit.

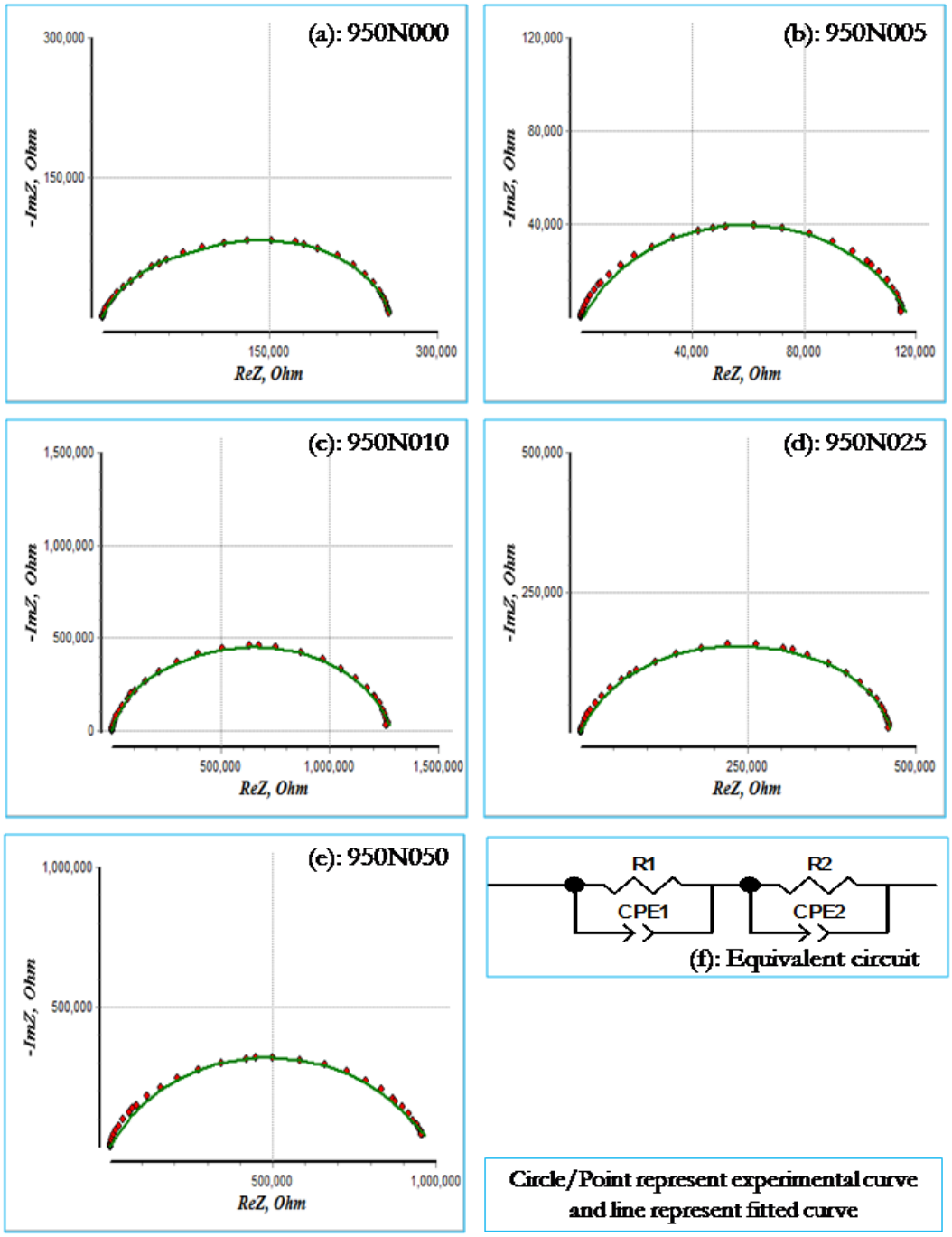

Figure 5.29: Impedance plots for the composition sintered at 950 °C and measurement done at 150 °C: (a) 950N000 (0.00 mol% Nb); (b) 950N005 (0.05 mol% Nb); (c) 950N010 (0.10 mol% Nb); (d) 950N025 (0.25 mol% Nb); (e) 950N050 (0.50 mol% Nb) and (f) Equivalent circuit.

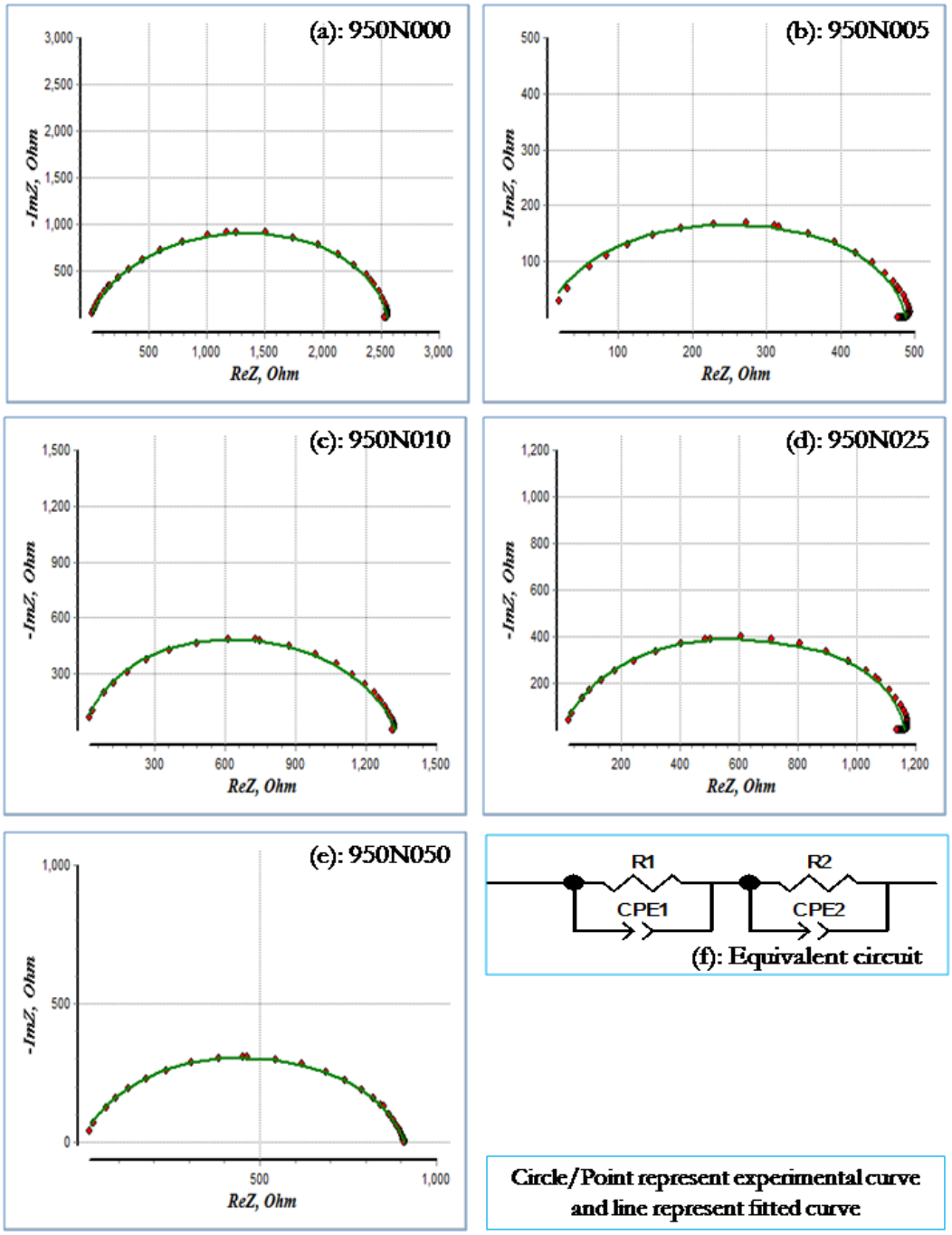

Figure 5.30: Impedance plots for the composition sintered at 950 °C and measurement done at 250 °C: (a) 950N000 (0.00 mol% Nb); (b) 950N005 (0.05 mol% Nb); (c) 950N010 (0.10 mol% Nb); (d) 950N025 (0.25 mol% Nb); (e) 950N050 (0.50 mol% Nb) and (f) Equivalent circuit.

The order of magnitude of the 'P' suggests that the semicircle is due to grain boundaries, typically of a double-layer effect [Jonscher (1977); Jorcin et al. (2006)]. Except 0.50 mol% Nb-doped sample sintered at 900 °C, which suggests that the semicircle is due to bulk grains. From Figs. 5.22 to 5.30 (f), R_1 and P_1 denote the resistance and capacitance/CPE is assigned to the high-frequency defects and/or adsorbed species at the grain boundary region, not necessarily at the same grain boundary; R_2 and P_2 represent the resistance and capacitance/CPE of the low-frequency grain boundary of most resistive elements that dominate the impedance results. The two R-values obtained at 50 °C, 150 °C & 250 °C are given in Tables 5.11-5.19 and were obtained by plot fitting. These values were further used to evaluate the apparent activation energy for charge transport through the grain boundary.

Figs. 5.22, 5.23, 5.24 and Tables 5.11, 5.12, 5.13 shows the total resistance given by R_T (Ω) = R_1 (Ω) + R_2 (Ω) of the samples sintered at 850 °C with different amounts of Nb_2O_5 measured at 50 °C, 150 °C & 250 °C. The R_T (Ω) measured for the 0.00, 0.05, 0.10, 0.25 and 0.50 mol% Nb_2O_5 doped ZnO-V_2O_5 samples sintered at 850 °C at 50 °C are $3.46x10^7$, $1.92x10^8$, $3.7x10^8$, $1.3x10^8$, $6.9x10^7$Ω; At 150 °C are $2.04x10^6$, $2.78x10^6$, $5.71x10^6$, $3.63x10^6$, $1.76x10^6$ Ω and at 250 °C are $1.69x10^4$, $4.24x10^4$, $1.29x10^5$, $8.38x10^4$, $6.61x10^4$ Ω respectively.

Table 5.10: Summary of fitted electrical parameter obtained from EIS software measured at 50 °C for Nb_2O_5 doped samples sintered at 850 °C.

Samples (50 °C)	R_1(Ω)	P_1	n_1	R_2(Ω)	P_2	n_2	R_T(Ω)
850N000	$1.17x10^6$	$1.42x10^{-9}$	0.92	$3.34x10^7$	$5.49x10^{-9}$	0.82	$3.46x10^7$
850N005	$7.56x10^7$	$6.70x10^{-9}$	0.70	$1.16x10^8$	$1.0x10^{-7}$	0.55	$1.92x10^8$
850N010	$1.54x10^8$	$2.13x10^{-9}$	0.72	$2.16x10^8$	$5.0x10^{-8}$	0.53	$3.7x10^8$
850N025	$3.44x10^7$	$9.55x10^{-9}$	0.67	$9.56x10^7$	$8.7x10^{-8}$	0.44	$1.3x10^8$
850N050	$1.36x10^6$	$1.26x10^{-9}$	0.93	$6.86x10^7$	$2.8x10^{-9}$	0.84	$6.9x10^7$

Table 5.11: Summary of fitted electrical parameter obtained from EIS software measured at 150 °C for Nb_2O_5 doped samples sintered at 850 °C.

Samples (150 °C)	$R_1(\Omega)$	P_1	n_1	$R_2(\Omega)$	P_2	n_2	$R_T(\Omega)$
850N000	$2.18x10^5$	$1.31x10^{-9}$	0.92	$1.82x10^6$	$6.77x10^{-9}$	0.85	$2.04x10^6$
850N005	$4.75x10^5$	$5.81x10^{-7}$	0.81	$2.31x10^6$	$6.24x10^{-9}$	0.73	$2.78x10^6$
850N010	$2.63x10^6$	$4.05x10^{-6}$	0.67	$3.08x10^6$	$3.54x10^{-9}$	0.72	$5.71x10^6$
850N025	$1.50x10^6$	$1.33x10^{-6}$	0.57	$2.14x10^6$	$8.79x10^{-9}$	0.72	$3.63x10^6$
850N050	$1.12x10^5$	$1.11x10^{-9}$	0.95	$1.65x10^6$	$2.77x10^{-9}$	0.87	$1.76x10^6$

Table 5.12: Summary of fitted electrical parameter obtained from EIS software measured at 250 °C for Nb_2O_5 doped samples sintered at 850 °C.

Samples (250 °C)	$R_1(\Omega)$	P_1	n_1	$R_2(\Omega)$	P_2	n_2	$R_T(\Omega)$
850N000	$2.57x10^3$	$1.57x10^{-8}$	0.82	$1.43x10^4$	$4.36x10^{-8}$	0.74	$1.69x10^4$
850N005	$6.10x10^3$	$1.07x10^{-5}$	0.98	$3.63x10^4$	$6.8x10^{-9}$	0.80	$4.24x10^4$
850N010	$7.60x10^4$	$1.7x10^{-5}$	0.55	$5.30x10^4$	$5.6x10^{-9}$	0.77	$1.29x10^5$
850N025	$3.81x10^4$	$3.02x10^{-5}$	0.54	$4.57x10^4$	$6.4x10^{-9}$	0.80	$8.38x10^4$
850N050	$3.29x10^4$	$3.66x10^{-9}$	0.83	$3.31x10^4$	$2.4x10^{-5}$	0.60	$6.61x10^4$

The total resistance R_T (Ω) measured at 50 °C for the sample doped with 0.10 mol% Nb_2O_5 is the maximum because of the small grain size; i.e., there are large number of grain boundaries.

Figs. 5.25, 5.26, 5.27 and Tables 5.14, 5.15, 5.16 shows the total resistance given by R_T (Ω) = R_1 (Ω) + R_2 (Ω) of the samples sintered at 900 °C with different amounts of Nb_2O_5 measured and calculated at 50 °C, 150 °C & 250 °C. The R_T (Ω) measured for the 0.00, 0.05, 0.10, 0.25 and 0.50 mol% Nb_2O_5 doped $ZnO\text{-}V_2O_5$ samples sintered at 900 °C at 50 °C are $1.46x10^7$, $4.64x10^8$, $2.53x10^8$, $2.65x10^8$, $5.36x10^9$ Ω; At 50 °C are $6.32x10^5$, $1.00x10^7$, $5.24x10^6$, $6.52x10^6$, $2.16x10^8$ Ω and at 250 °C are $1.48x10^4$, $9.42x10^4$, $5.28x10^4$, $5.75x10^4$, $1.17x10^6$ Ω respectively. The resistivity of a polycrystalline material decreases with the increase in grain size due to the decrease in the grain boundary number. Therefore, we found that the Nb_2O_5 containing sample has a higher value of resistivity than the binary $ZnO\text{-}V_2O_5$ varistor.

Table 5.13: Summary of Fitted Electrical parameter obtained from EIS software measured at 50 °C for Nb_2O_5 doped samples sintered at 900 °C.

Samples (50 °C)	R_1 (Ω)	P_1	n_1	R_2 (Ω)	P_2	n_2	R_T (Ω)
900N000	$2.57x10^6$	$4.49x10^{-9}$	0.90	$1.21x10^7$	$1.9x10^{-8}$	0.79	$1.46x10^7$
900N005	$1.07x10^8$	$9.81x10^{-10}$	0.95	$3.57x10^8$	$2.7x10^{-9}$	0.93	$4.64x10^8$
900N010	$4.15x10^7$	$1.88x10^{-9}$	0.93	$2.11x10^8$	$3.8x10^{-9}$	0.91	$2.53x10^8$
900N025	$4.87x10^7$	$1.86x10^{-9}$	0.93	$2.16x10^8$	$1.3x10^{-9}$	0.94	$2.65x10^8$
900N050	$7.45x10^8$	$3.26x10^{-11}$	0.91	$4.62x10^9$	$5x10^{-11}$	0.95	$5.36x10^9$

Table 5.14: Summary of fitted electrical parameter obtained from EIS software measured at 150 °C for Nb_2O_5 doped samples sintered at 900 °C.

Samples (150 °C)	R_1 (Ω)	P_1	n_1	R_2 (Ω)	P_2	n_2	R_T (Ω)
900N000	$1.89x10^5$	$5.28x10^{-9}$	0.90	$4.43x10^5$	$3.94x10^{-8}$	0.79	$6.32x10^5$
900N005	$2.30x10^6$	$1.16x10^{-9}$	0.95	$7.73x10^6$	$4.43x10^{-9}$	0.92	$1.00x10^7$
900N010	$6.34x10^5$	$1.32x10^{-9}$	0.96	$4.60x10^6$	$5.27x10^{-9}$	0.93	$5.24x10^6$
900N025	$1.22x10^6$	$1.40x10^{-9}$	0.95	$5.30x10^6$	$2.80x10^{-9}$	0.92	$6.52x10^6$
900N050	$2.34x10^7$	$5.52x10^{-11}$	0.90	$1.92x10^8$	$1.80x10^{-10}$	0.88	$2.16x10^8$

Table 5.15: Summary of fitted electrical parameter obtained from EIS software measured at 250 °C for Nb_2O_5 doped samples sintered at 900 °C.

Samples (250 °C)	R_1 (Ω)	P_1	n_1	R_2(Ω)	P_2	n_2	R_T (Ω)
900N000	$2.35x10^3$	$1.20x10^{-8}$	0.92	$1.25x10^4$	$1.55x10^{-8}$	0.85	$1.48x10^4$
900N005	$2.41x10^4$	$1.97x10^{-9}$	0.94	$7.01x10^4$	$6.25x10^{-9}$	0.90	$9.42x10^4$
900N010	$1.33x10^4$	$1.98x10^{-9}$	0.96	$3.96x10^4$	$6.56x10^{-9}$	0.91	$5.28x10^4$
900N025	$1.54x10^4$	$2.51x10^{-9}$	0.93	$4.21x10^4$	$7.14x10^{-9}$	0.88	$5.75x10^4$
900N050	$6.06x10^5$	$1.10x10^{-10}$	0.88	$5.63x10^5$	$1.11x10^{-9}$	0.81	$1.17x10^6$

The total resistance R_T (Ω) for the sample doped with 0.50 mol% Nb_2O_5 is the maximum because the order of magnitude of the 'P' suggests that the semicircle is due to bulk grain. 0.50 mol% Nb doping increases the grain resistance as well

as grain size. Overall grain resistance is significant in comparison to grain boundary for the sample doped with 0.50 mol% Nb_2O_5.

Figs. 5.28, 5.29, 5.30 and Tables 5.17, 5.18, 5.19 shows the total resistance given by R_T (Ω) = R_1 (Ω) + R_2 (Ω) measured at 50 °C, 150 °C & 250 °C of the samples sintered at 950 °C with different amounts of Nb_2O_5. The R_T (Ω) for the 0.00, 0.05, 0.10, 0.25 and 0.50 mol% Nb_2O_5 doped ZnO-V_2O_5 samples measured at 50 °C are $3.97x10^6$, $6.12x10^7$, $5.36x10^7$, $8.23x10^7$, $2.59x10^7$ Ω; At 150 °C are $2.56x10^5$, $1.13x10^5$, $1.24x10^6$, $4.49x10^5$, $1.01x10^6$ Ω and at 250 °C are $2.56x10^3$, $4.93x10^2$, $1.33x10^3$, $1.17x10^3$, $9.10x10^2$ Ω respectively. The Nb_2O_5 containing samples sintered at 950 °C have a higher value of resistivity than the binary ZnO-V_2O_5 varistor. Since, the resistivity of a polycrystalline material decreases with the increase in grain size and the decrease in the grain boundary number.

Table 5.16: Summary of fitted electrical parameter obtained from EIS software measured at 50 °C for Nb_2O_5 doped samples sintered at 950 °C.

Samples (50 °C)	R_1 (Ω)	P_1	n_1	R_2 (Ω)	P_2	n_2	R_T (Ω)
950N000	$3.20x10^5$	$1.33x10^{-8}$	0.89	$3.65x10^6$	$3.7x10^{-8}$	0.85	$3.97x10^6$
950N005	$7.20x10^6$	$2.42x10^{-9}$	0.91	$5.40x10^7$	$1.1x10^{-8}$	0.86	$6.12x10^7$
950N010	$8.29x10^6$	$1.8x10^{-9}$	0.92	$4.54x10^7$	$4.2x10^{-9}$	0.90	$5.36x10^7$
950N025	$1.40x10^7$	$1.82x10^{-9}$	0.92	$6.83x10^7$	$9.6x10^{-9}$	0.88	$8.23x10^7$
950N050	$1.14x10^7$	$2.41x10^{-8}$	0.56	$1.45x10^7$	$3.6x10^{-7}$	0.75	$2.59x10^7$

Table 5.17: Summary of fitted electrical parameter obtained from EIS software measured at 150 °C for Nb_2O_5 doped samples sintered at 950°C.

Samples (150 °C)	R_1 (Ω)	P_1	n_1	R_2 (Ω)	P_2	n_2	R_T (Ω)
950N000	$4.68x10^4$	$1.85x10^{-8}$	0.89	$2.09x10^5$	$4.84x10^{-8}$	0.85	$2.56x10^5$
950N005	$1.31x10^4$	$1.5x10^{-9}$	0.99	$9.98x10^4$	$6.41x10^{-9}$	0.89	$1.13x10^5$
950N010	$2.27x10^5$	$1.36x10^{-9}$	0.96	$1.01x10^6$	$2.63x10^{-9}$	0.94	$1.24x10^6$
950N025	$7.56x10^4$	$1.61x10^{-9}$	0.96	$3.74x10^5$	$4.41x10^{-9}$	0.92	$4.49x10^5$
950N050	$8.19x10^4$	$3.22x10^{-6}$	0.41	$9.27x10^5$	$9.29x10^{-9}$	0.75	$1.01x10^6$

Table 5.18: Summary of fitted electrical parameter obtained from EIS software measured at 250 °C for Nb_2O_5 doped samples sintered at 950°C.

Samples (250 °C)	R_1 (Ω)	P_1	n_1	R_2 (Ω)	P_2	n_2	R_T (Ω)
950N000	$3.64x10^2$	$3.82x10^{-8}$	0.89	$2.20x10^3$	$5.47x10^{-8}$	0.84	$2.56x10^3$
950N005	$1.42x10^2$	$5.33x10^{-9}$	0.99	$3.50x10^2$	$2.3x10^{-7}$	0.70	$4.93x10^2$
950N010	$2.96x10^2$	$2.24x10^{-9}$	0.99	$1.03x10^3$	$2.5x10^{-8}$	0.80	$1.33x10^3$
950N025	$1.31x10^2$	$4.81x10^{-9}$	0.99	$1.04x10^3$	$4.5x10^{-8}$	0.78	$1.17x10^3$
950N050	$3.23x10^2$	$9.11x10^{-8}$	0.84	$5.87x10^2$	$2.3x10^{-8}$	0.81	$9.10x10^2$

Figs. 5.31. 5.32 & 5.33 (a-e) present the Arrhenius plots of the R_1 and R_2 regions for high and low frequencies respectively. These figures show the presence of two linear regions with different slopes. The slope change in the two cases occurs at ~100 °C/150 °C. Tables 5.20, 5.21 & 5.22 presents the activation energies for the two processes as a function of Nb_2O_5 doped samples calculated from the data presented in Figs. 5.31. 5.32 & 5.33. The resistance data in both R_1 and R_2 regions follow the Arrhenius law [Pandey et al. (2007)]

$$R = R_0 \, exp\left(-\frac{E_a}{RT}\right) \tag{5.4}$$

where E_a is the activation energy for conduction, k_B is the Boltzmann's constant and R_0 is the pre-exponential factor. The least square fitting method of the resistance data were used to calculate the activation energies 'Ea' of conduction. The temperature dependence of the R_1 and R_2 regions shows considerable complexity.

Fig. 5.31 shows the curvature in the Arrhenius plots and activation energy of 0.223 to 0.410 eV below approximately 100 °C/150 °C. Above 100 °C/150 °C, the activation energies were from in the range of 0.831 to 1.022 eV, this is because of the varistor action is critically dependent on the presence of excess oxygen (as well as V) at ZnO-ZnO interfaces and the activation energies with varying temperature. The level of 0.223 to 0.410 eV is related to the charge state of interstitial oxygen $O_i^{-1}$and O_i^0. Form Table 5.19, for the 0.00 mol% (850N000), 0.05 mol% (850N005), 0.10 mol% (850N010), 0.25 mol% (850N025) and 0.50

mol% (850N050) Nb-doped sample sintered at 850 °C for 3 h, the Ea values are 0.223, 0.381, 0.410, 0.335, 0.343 eV and 0.340, 0.352, 0.389, 0.340, 0.329 eV for the R_1 and R_2 grain boundaries regions, respectively. In relation to the nature of the interface states, two types of grain boundary junctions have been suggested, ZnO–ZnO homojunction (0.223 to 0.410 eV) and ZnO-V_2O_5-ZnO heterojunction (0.831 to 1.022 eV), as defined by impedance spectroscopy [West et al. (1997)]. It is quite possible that the compositions of the V-rich intergranular phases responsible for the interface states in ZnO varistors are varied with doping constituents and heat-treatment conditions [Chen et al. (2015); Wu et al. (2011)]. Consequently, it is reasonable to assign an energy level of 0.223 to 0.410 eV to the interface state of ZnO-intergranular phase heterojunction modified by Nb [Nahm et al. (2007); (2009); (2011); (2015)].

Fig. 5.32 shows the curvature in the Arrhenius plots and activation energy of 0.289 to 0.485 eV below approximately 100°C. Above 100 °C, the activation energies were found in the range of 0.757 to 1.07 eV, that is because of varistor action is critically dependent on the presence of excess oxygen (as well as V) at ZnO-ZnO interfaces and the activation energies with varying temperature. The level of 0.289 to 0.485 is related to the charge state of interstitial oxygen $O_i^{-1}$and O_i^0. Form Table 5.20, for the 0.00 mol% (900N000), 0.05 mol% (900N005) 0.10 mol% (900N010), 0.25 mol% (900N025) and 0.50 mol% (900N050) Nb-doped sample sintered at 900°C for 3 h, the Ea values below 100°C are 0.289, 0.438, 0.485, 0.421, 0.399 eV and 0.363, 0.421, 0.445, 0.413, 0.369 eV for the R_1 and R_2 grain boundaries regions, respectively. In relation to the nature of the interface states, two types of grain boundary junctions have been suggested that is ZnO–ZnO homojunction (0.289 to 0.485 eV) and ZnO-V_2O_5-ZnO heterojunction (0.757 to 1.07 eV), as defined by impedance spectroscopy [West et al. (1997)]. It is quite possible that the compositions of the V-rich intergranular phases responsible for the interface states in ZnO varistors are varied with doping constituents and heat-treatment conditions [Chen et al. (2015); Wu et al. (2011)]. Consequently, it is reasonable to assign an energy level of 0.289 to 0.485 eV to the interface state

of ZnO intergranular phase heterojunction modified by Nb [Nahm et al. (2007); (2009); (2011); (2015)].

Fig. 5.33 shows the curvature in the Arrhenius plots and activation energy of 0.182 to 0.417 eV below approximately 100 °C. Above 100 °C, the activation energies were found in the range of 0.849 to 1.275 eV that is because of varistor action is critically dependent on the presence of excess oxygen (as well as V) at ZnO-ZnO interfaces and the activation energies vary with temperature. The level of 0.182 to 0.417 eV is related to the charge state of interstitial oxygen $O_i^{-1}$and O_i^0. Form Table 5.21, for the 0.00 mol% (950N000), 0.05 mol% (950N005), 0.10 mol% (950N010), 0.25 mol% (950N025) and 0.50 mol% (950N050) Nb-doped sample sintered at 950 °C for 3 h, the Ea values below 100°C are 0.217, 0.272, 0.397, 0.385, 0.341 eV and 0.328, 0.338, 0.417, 0.344, 0.182 eV for the R_1 and R_2 grain boundaries regions respectively. In relation to the nature of the interface states, two types of grain boundary junctions have been suggested that is ZnO–ZnO homojunction (0.182 to 0.417 eV) and ZnO-V_2O_5-ZnO heterojunction (0.849 to 1.275 eV), as defined by impedance spectroscopy [West et al. (1997)]. It is quite possible that the compositions of the V-rich intergranular phases responsible for the interface states in ZnO varistors are varied with doping constituents and heat-treatment conditions [Chen et al. (2015); Wu et al. (2011)]. Consequently, it is reasonable to assign an energy level of 0.182 to 0.417 eV to the interface state of ZnO intergranular phase heterojunction modified by Nb [Nahm et al. (2007); (2009); (2011); (2015)].

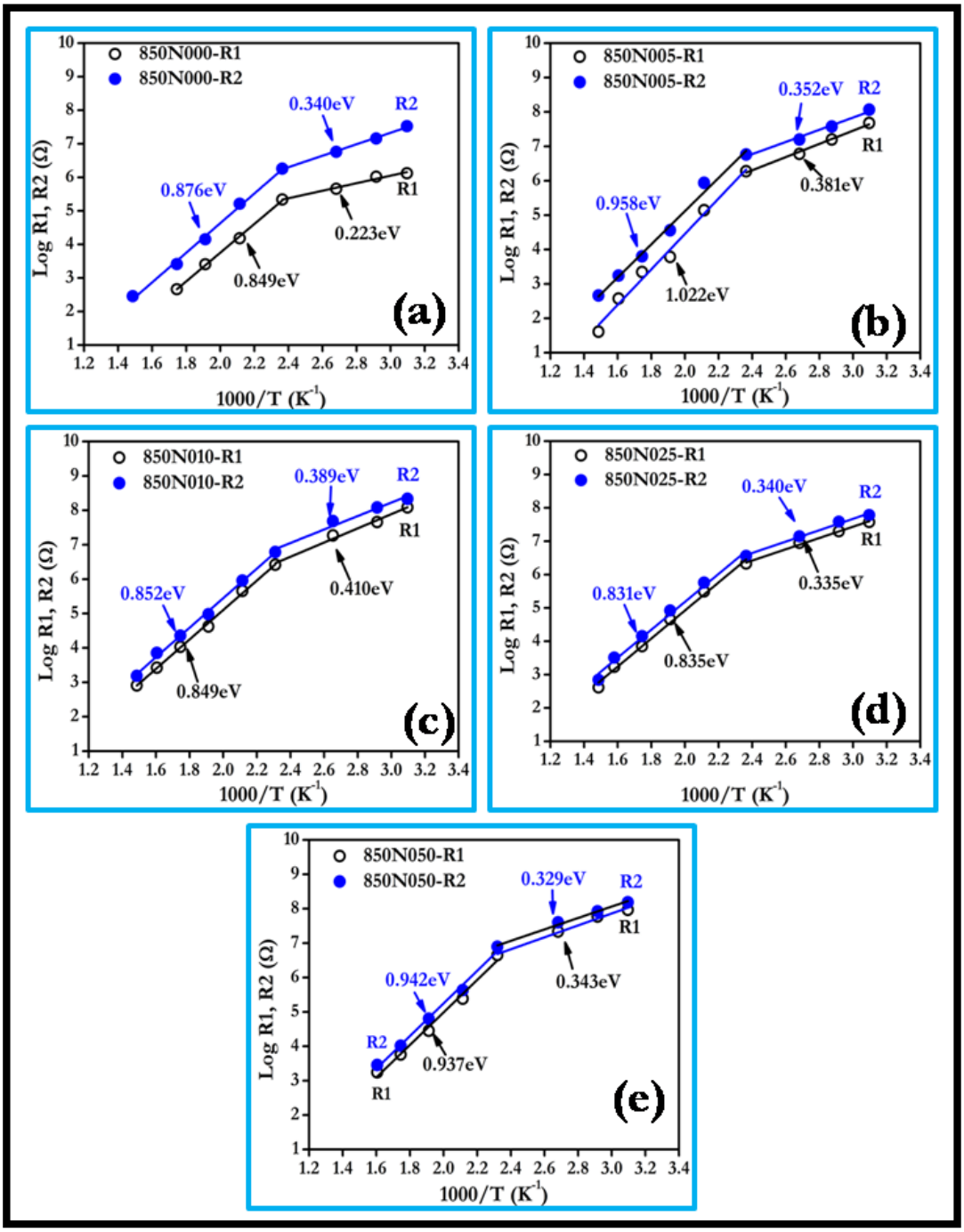

Figure 5.31: Arrhenius plots for resistance R_1 and R_2 of composition sintered at 850 °C: (a) 850N000 (0.00 mol% Nb); (b) 850N005 (0.05 mol% Nb); (c) 850N010 (0.10 mol% Nb); (d) 850N025 (0.25 mol% Nb) and (e) 850N050 (0.50 mol% Nb).

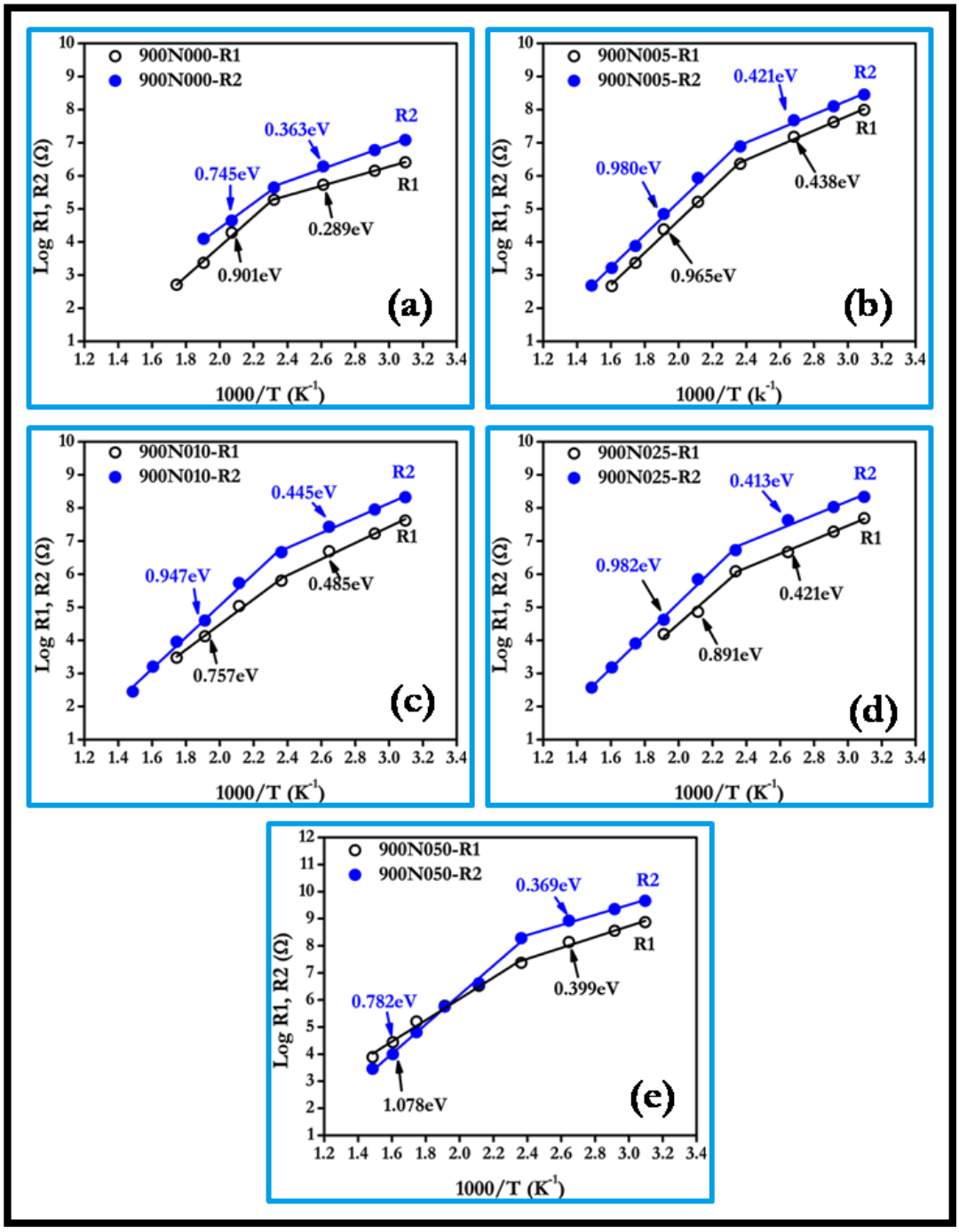

Figure 5.32: Arrhenius plots for resistance R_1 and R_2 of composition sintered at 900 °C: (a) 950N000 (0.00 mol% Nb); (b) 950N005 (0.05 mol% Nb); (c) 950N010 (0.10 mol% Nb); (d) 950N025 (0.25 mol% Nb) and (e) 950N050 (0.50 mol% Nb).

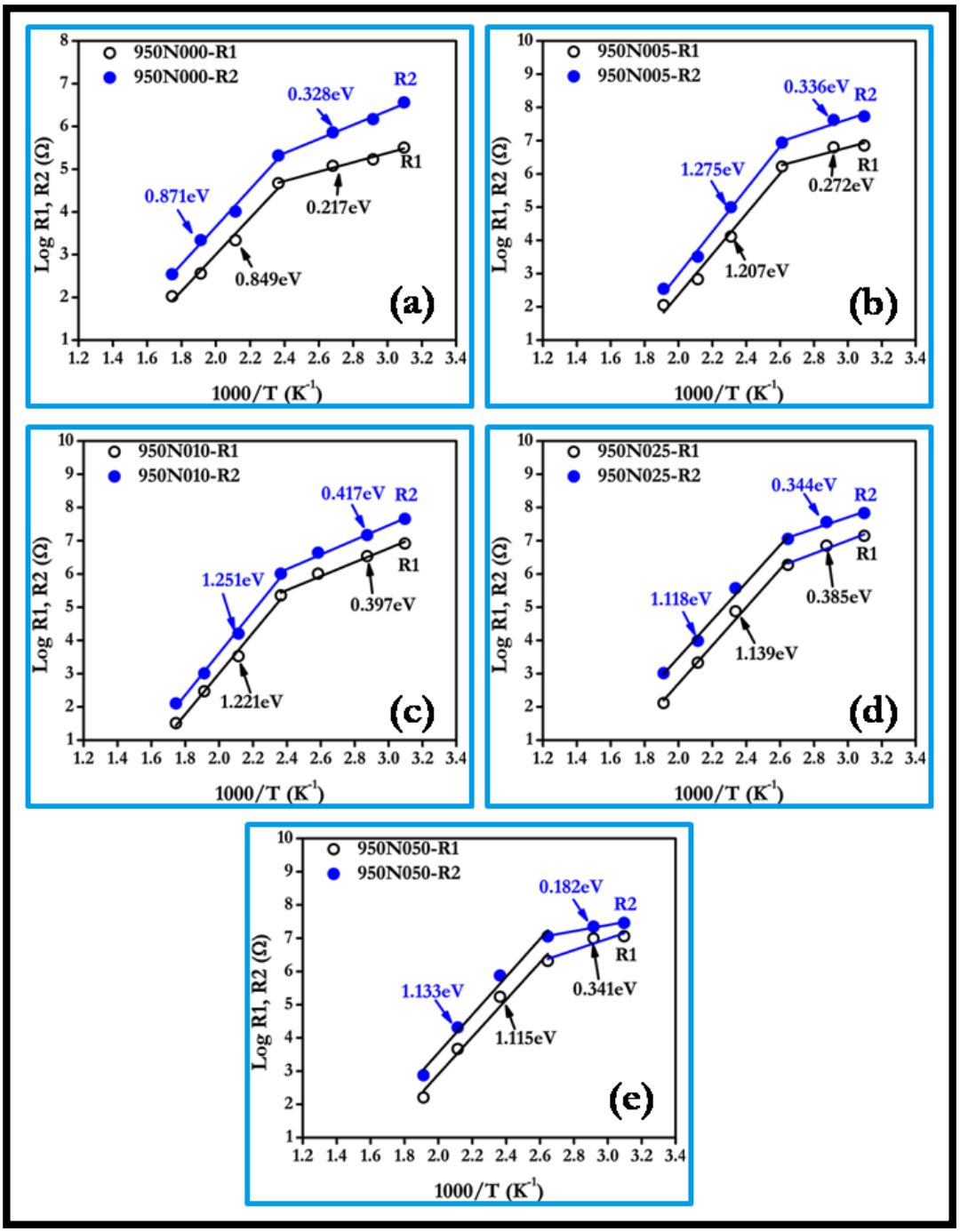

Figure 5.33: Arrhenius plots for resistance R_1 and R_2 of composition sintered at 950 °C: (a) 950N000 (0.00 mol% Nb); (b) 950N005 (0.05 mol% Nb); (c) 950N010 (0.10 mol% Nb); (d) 950N025 (0.25 mol% Nb) and (e) 950N050 (0.50 mol% Nb).

Table 5.19: Activation energies calculated from the Arrhenius plot at low and high frequency region for the samples sintered at 850 °C.

Samples	$R_1 : E_1$: (eV)		$R_2 : E_2$: (eV)	
	T<150 °C	T>150 °C	T<150 °C	T>150 °C
850N000	0.223	0.849	0.340	0.876
850N005	0.381	1.022	0.352	0.958
850N010	0.410	0.851	0.389	0.852
850N025	0.335	0.835	0.340	0.831
850N050	0.343	0.937	0.329	0.942

Table 5.20: Activation energies calculated from the Arrhenius plot at low and high frequency region for the samples sintered at 900 °C.

Samples	$R_1 : E_1$: (eV)		$R_2 : E_2$: (eV)	
	T<150 °C	T>150 °C	T<150 °C	T>150 °C
900N000	0.289	0.901	0.363	0.745
900N005	0.438	0.965	0.421	0.98
900N010	0.485	0.757	0.445	0.947
900N025	0.421	0.891	0.413	0.982
900N050	0.399	0.782	0.369	1.07

Table 5.21: Activation energies calculated from the Arrhenius plot at low and high frequency region for the samples sintered at 950 °C.

Samples	$R_1 : E_1$: (eV)		$R_2 : E_2$: (eV)	
	T<150°C	T>150°C	T<150°C	T>150°C
950N000	0.217	0.849	0.328	0.871
950N005	0.272	1.207	0.338	1.275
950N010	0.397	1.221	0.417	1.251
950N025	0.385	1.139	0.344	1.118
950N050	0.341	1.115	0.182	1.133

The non-linear property of the varistors is explained by the existence of potential barrier at the grain boundaries. In practice, there are a variety of inter-grain conduction paths that operate in parallel in varistor. They operate through the grain boundary region or through the bulk inter-granular material. In fact, transition metal oxides are involved in the formation of interfacial states and deep bulk traps at grain boundaries, providing large potential barriers to give better nonlinear characteristics. This barrier is schottky-type. In which, conduction in linear region is dominated by thermionic emission over this Schottky barrier. Thus it is clear that vanadium ions play an important role in the non-linear conductivity of the prepared ceramics and it is important to discuss the defect chemistry induced by doping ZnO with V_2O_5 [Hng et al. (1999); (2000)].

ZnO is well known for its non-stoichiometry due to the zinc atoms interstitial sites and exhibits oxygen vacancies. These defects introduce donor states in the forbidden band, slightly below the conducting band. The donors are assumed to be interstitial zinc ions Zn^i. Using Kroger–Vink notation, we can write:

$$Zn_i^x \rightarrow e' + Zn_i^0 \tag{5.5}$$

$$Zn_i^0 \rightarrow e' + Zn_i^{00} \tag{5.6}$$

where Zn_i^0 and Zn_i^{00} are once and twice ionized interstitial zinc atoms respectively. Such free electrons (e') moves to the conducting band and enhances the ZnO conductivity which can be further increased by the extrinsic defects. But when ZnO is doped with V_2O_5, a part of the V_2O_5 additive have dissolved into the ZnO matrix and V^{5+} ions enter the interstitial sites of ZnO structure. Therefore, a substitutional reaction was believed to occur as below:

$$V_2O_5 \xrightarrow{ZnO} 2V_{Zn}^{000} + 2O_0 + \frac{3}{2}O_2 + 6e' \tag{5.7}$$

or

$$V_2O_5 \xrightarrow{ZnO} 2V_{Zn}^{000} + 2V_{Zn}^{2} + 5O_0 \tag{5.8}$$

Eq. (5.7) is an electron compensation reaction and the Eq. (5.8) is a defect compensation reaction. As there are more donors induced in ZnO–V_2O_5 than the intrinsic ones in ZnO, the electron compensation reaction seems more likely to have occurred. V_{Zn} is vanadium atom in zinc atom substitution site. In Zn substitutions with vanadium atoms, free electrons are released and raise the conductivity by increasing electron density. Thus increase in conductivity was observed with increase in V_2O_5 content. Moreover, the zinc vacancies distribute preferably near the grain boundaries for a relaxation of the high strain induced by the vacancies. A schottky barrier might thus be induced by such a concentration gradient of defects created at the grain boundaries for the ZnO–V_2O_5 system. It should be mentioned that the barrier height depends on the applied voltage and vanishes above certain field strength. Also the barrier decreases with increase in grain conductivity and collapses when the grain conductivity is too high [Levinson (1979); Hng et al. (1999); (2000)].

From the Figs. 5.31, 5.32 & 5.33, it is observed that there is a decrease in resistance with increasing temperature. It could be attributed to negative temperature coefficient of resistance and semiconducting behavior of Nb_2O_5 doped ZnO-V_2O_5 systems, obeying $R=R_O\, e^{-Ea/KT}$ in the temperature range of 50 to 400 °C. The resistance of Nb_2O_5 doped ZnO varistor falls suddenly in linear fashion up to certain transition temperature and after that the resistance decreases exponentially with increasing temperature. The transition temperature depends on doping concentration as well as sintering temperature.

From Arrhenius plot, it is observed that the curve for ZnO-V_2O_5-Nb_2O_5 systems have low temperature region and high temperature region. The change in slope of the graph, from one region to other region occurs between two temperatures depending upon the sintering temperature as well as the amount of Nb_2O_5 doping in ZnO-V_2O_5 varistor. The transition temperatures for the Nb_2O_5 doping in ZnO-V_2O_5varistor with 0.00 mol%, 0.05 mol%, 0.10 mol%, 0.25 mol% and 0.50 mol% Nb_2O_5 doping are 100˚C/150˚C.

From R-T graphs, it has been observed that the resistance of sample is more depend upon the doping concentration as compared to the varing sintering temperature 850 °C to 950 °C. The effect of Nb_2O_5 on the electrical properties of ZnO based resistors can be analyzed with grain boundary barrier model for ZnO based resistors. The defects generated by the presence of Nb_2O_5 (as Nb^{5+}) are fundamental in the formation of depletion layers at the grain boundaries. It leads to the creation of potential barriers when compensated by the negative charges at the grain boundary interface [Levinson et al. (1979)]. Because the ionic radii of Nb^{5+} (0.070 nm) and Zn^{2+} (0.074nm) are almost same, so that Nb^{5+} will occupy the Zn^{2+} sites in the depletion layer at the grain boundary for 0.50 mol% Nb_2O_5 doping. The following reaction occur-

$$Nb_2O_5 \overset{ZnO}{\longleftrightarrow} 2Nb_{Zn} + 2O_O + \frac{3}{2}O_2(g) \tag{5.9}$$

$$Nb_{Zn} \leftrightarrow Nb_{Zn}^{3+} + 3e \tag{5.10}$$

Therefore the 0.50 mol% Nb_2O_5 doping increased the donor concentration in the depletion layer at the grain boundary and thereby decreased the resistance.

From 0.05 to 0.25 mol% Nb_2O_5 doping, it can be assumed that the niobium ions begin to occupy the interstitial sites which would otherwise be occupied by interstitial zinc ions. At this time, niobium behaves as an acceptor,

$$\frac{1}{2}Nb_2O_5 \overset{ZnO}{\longleftrightarrow} 2Nb_1^{3'} + 3h' + \frac{5}{4}O_2(g) \tag{5.11}$$

Thus the electrons generated in equation (5.10) are absorbed as a result of $Nb_1^{3'}$ formation. This causes the donor concentration to decreases and therefore the resistivity increases. Doping of 0.05 to 0.25 mol% Nb_2O_5 causes the Nb_2O_5 dopant to segregate at the grain boundary. Further increases in the amount of Nb_2O_5 doping, it is easy for the ions to migrate at the grain boundary. This decreases the surface state density at the grain boundary and results in a fall of the barrier height. Therefore the resistivity decreases [Gupta et al. (1979)].

The values of E_a obtained correspond to typical hopping energy values between variable valence ions of the same dopant (Nb). Slightly higher values of activation energies for grain boundaries are due to more disordered nature of grain boundaries. Nb can exist in three variable valence states of +3, +4 and +5 depending on temperature of heat treatment. There may be larger concentration of Nb in variable valence states. [Pandey et al. (2007)]. During heating, the solubility of Nb ions was increased because of the lower ionic radii. As a result, more Nb ions were segregated in the grain boundaries and improved the non-linearity characteristics. Temperature behavior of the impedance data can be described as follows: For temperatures lower than 100°C, the presence of $V_o^{\cdot\cdot}$ or $Zn_i^{\cdot\cdot}$ may be related with the low and high frequency time constants, respectively. Physically adsorbed water should be ruled out once the varistor system is dense. For higher temperatures, O' and O" are the main adsorbed species at the grain boundary.

Summary: The present chapter discussed the influence of the Nb_2O_5 content on the structure and the electrical response of $ZnO–V_2O_5$ based varistors ceramics. Samples were prepared via solid state reaction at sintering temperature of 850 °C, 900 °C & 950 °C. The microstructure of the Nb_2O_5-doped $ZnO–V_2O_5$ varistors consisted of ZnO grain as the primary phase and $Zn_3(VO_4)_2$ as the minor secondary phases, which acts as liquid-phase sintering promoter and has a significant effect on the sintered density. The average grain size of the $ZnO–V_2O_5$ system sintered at 850 to 950°C was found to be in range of 3.8 to 16.6 μm, which depend upon the amount of Nb_2O_5 doping. The 0.10 mol% Nb doped $ZnO–V_2O_5$ sample sintered at 900°C exhibited the most optimum grain size of 7.0μm. EDS spectra of ZnO grain boundary show V and Nb segregation in the samples. Among all of the samples, the 0.50 mol% Nb-doped sample sintered at 900°C was found to have the highest values of total resistance. The 0.10 mol% Nb-doped system sintered at 900°C exhibited the highest nonlinear coefficient of 7.1, the highest breakdown field value of 281.5 V/mm, the lowest leakage current density of J_L = 310.577 μA/cm^2, the έ (1kHz) = 719 and the lowest tan δ (1kHz) = 0.079 among all of the samples. Ea values below 150°C for 0.10 mol% Nb-doped samples sintered at 900°C were found to be 0.485 and 0.445 eV for the R_1 (high frequency) and R_2 (low frequency) grain boundary regions, respectively. Conclusively, among all of the Nb doped $ZnO–V_2O_5$ samples, it was found that the 0.10 mol% Nb-doped samples sintered at 900°C is a candidate material for use in chip varistors.

The next chapter discusses about the effect of MnO doping on $ZnO–V_2O_5–Nb_2O_5$ based ceramics systems synthesized via solid state technique and sintered from 850 to 950 °C on the structure and the influence of the grain boundary structure on the electrical properties of ZnO based ceramics in a systematic manner using AC impedance and dielectric spectroscopy (IS) have been analyzed. Various properties investigated include phase, microstructure, density, dielectric and Non-linear properties respectively.